Pacific Northwest
NATIONAL LABORATORY

PNNL-36737

Preliminary Characterization and Evaluation on ShAPE Manufactured 316H and ODS Steels

M3CR-22PN0402023

September 2024

Isabella van Rooyen
Mageshwari Komarasamy
Chinthaka Silva
Tanvi Ajantiwalay
Quin R S Miller
Ramprashad Prabhakaran
Shalini Tripathi
Julian Atehortua
Mayor Pole
David Garcia
Matthew Olszta
Tianhao Wang

U.S. DEPARTMENT OF ENERGY

Prepared for the U.S. Department of Energy
under Contract DE-AC05-76RL01830

DISCLAIMER

PACIFIC NORTHWEST NATIONAL LABORATORY
operated by
BATTELLE
for the
UNITED STATES DEPARTMENT OF ENERGY
under Contract DE-AC05-76RL01830

Printed in the United States of America

Available to DOE and DOE contractors from
the Office of Scientific and Technical Information,
P.O. Box 62, Oak Ridge, TN 37831-0062
www.osti.gov
ph: (865) 576-8401
fox: (865) 576-5728
email: reports@osti.gov

Available to the public from the National Technical Information Service
5301 Shawnee Rd., Alexandria, VA 22312
ph: (800) 553-NTIS (6847)
or (703) 605-6000
email: info@ntis.gov
Online ordering: http://www.ntis.gov

PNNL-36737

Preliminary Characterization and Evaluation on ShAPE Manufactured 316H and ODS Steels

M3CR-22PN0402023

September 2024

Isabella van Rooyen
Mageshwari Komarasamy
Chinthaka Silva
Tanvi Ajantiwalay
Quin R S Miller
Ramprashad Prabhakaran
Shalini Tripathi
Julian Atehortua
Mayor Pole
David Garcia
Matthew Olszta
Tianhao Wang

Prepared for
the U.S. Department of Energy
under Contract DE-AC05-76RL01830

Pacific Northwest National Laboratory
Richland, Washington 99354

Summary

This study provides the first- of- a- kind results of direct tube formation through shear assisted processing and extrusion (ShAPE) for oxide dispersion strengthened (ODS) steel material; previously only bar was successfully made.

The Advanced Materials and Manufacturing Technologies (AMMT) program develops cross-cutting technologies in support of a broad range of nuclear reactor technologies and maintains U.S. leadership in materials and manufacturing technologies for nuclear energy applications. The overarching vision of AMMT is to accelerate the development, qualification, demonstration, and deployment of advanced materials and manufacturing technologies to enable reliable and economical nuclear energy.

Solid-state advanced manufacturing techniques can overcome some of the challenges in liquid-based additive manufacturing processes and should therefore be considered in material design and manufacturing as well. The work presented in this report forms part of a study on solid-state additive manufacturing techniques of 316 stainless steels and ODS steel components and supports the vision and goals of the AMMT program relevant to accelerate the development and deployment of advanced manufacturing processes. Achieving this can provide a safety improvement through larger safety margins, economic benefit for higher efficiency during operation, and a cost reduction through more effective manufacturing processes and less waste.

This study provides preliminary information on development of shear-assisted processing and extrusion tube forming of ODS directly from stock material, and not via an interim step of bar and pilgering as one of the current manufacturing methodologies. These experiments also aimed to determine the sensitivity towards mechanical alloyed ODS powder, as previously, the successful bar feedstock manufacturing was performed with highly specialized spherodized powder. The full solid-state manufacturing feasibility study will be completed and reported in a final feasibility evaluation during 2025. The study investigation used two types of ODS steel feedstock billets namely 1) uncrystallized ODS PM2000 alloy ($Fe_{20}Cr_5Al$) purchased from Plansee USA LLC and 2) spark plasma sintered (SPS) billets fabricated for the AMMT program from 14YWT powder (batch unique identifier 14YWT-V540-01-40H 3) funded by the U.S. Department of Energy's Global Nuclear Energy Partnership program in 2008 subcontract-70553-001-09. The benefit of using this powder is that the result of the properties obtained from the advanced manufacturing techniques used in this study, can be benchmarked. This benchmark comparison will be performed in the final phase of this project.

The first ShAPE experiment completed on the PM2000 billet yielded an approximately 4-inch length of tube and shows in principle the feasibility of the direct tube fabrication in a single step while recognizing that full steady-state conditions were not reached during the first experiment and that process optimization should still be performed on this specific material conditions. A detailed microstructural analysis, although showing variations between the start, middle, and end sections, shows that conditions towards the end were more consistent and can be built upon during subsequent studies. However, the results, both in understanding the process parameters and behavior in relationship with the microstructural variations, can provide valid input to the modeling efforts, although not funding under AMMT program, can minimize future experiments. Specific observations form the PM2000 extrudate tube as follows:

- Al- and Y-rich secondary precipitates, Al_2O_3 and/or $(Al,Y)_2O_3$ type oxides, and elemental Ti-rich particles could be identified from electron microscopy analysis.
- Precipitate size increases during the SHAPE process to approximately double the base material size although the precipitate sizes of the end section are smaller than the mid-section.
- The number density of precipitates shows an inverse proportionality to the change of their size, except for the bulky square-type Al-rich precipitates mostly identified at the end section of the ShAPE sample. The increase in precipitate size and decrease in density suggest ShAPE-induced growth of the secondary oxide particles but without significantly affecting the overall level of oxidation. This suggests that ShAPE might be used to refine ODS particles, but further experimentation is required to verify this observation. However, the moderate size and the highest density of bulky square-type precipitates observed at the end section of the extruded sample also suggest ShAPE-induced increase in the second phase precipitation.

Compared to the wrought PM2000, all the experiments with SPS billets as feedstock had resulted in fractured tubes. This could be due to the porosity in the SPS consolidated feedstocks. An early conclusion is therefore that the stock material for the current feasibility shows that less than 97% dense feedstock is not sufficient for ODS materials for direct tube forming. However, another aspect that needs to be considered that has not been established yet is how the bimodal grain sizes influence the consistency and flow during the extrusion process. Characterization of these extrudates could not yet be performed to determine if there are any differences in the ODS particle size or distributions after exposed to the combined effect of SPS and ShAPE extrusion. Specifically, the third experiment using SPS billet 4, did not reach steady state; therefore, the resulting microstructure would not provide conclusive evidence yet.

Finally, the four ShAPE experiments conducted show feasibility regarding fabricability for ODS tube forming was shown although optimization for microstructure repeatability would need to receive attention with follow up work therefore the combination of results reported here, together with the separate studies by other PNNL researchers on bar fabrication of ODS, provide the justification for early TRL feasibility.

Acknowledgments

The research presented here was supported by the Advanced Materials and Manufacturing Technologies Program of the Department of Energy's (DOE's) Office of Nuclear Energy. PNNL is a multiprogram national laboratory operated for DOE by Battelle Memorial Institute under Contract No. DE-AC05-76RL01830. PNNL would like to thank Dr Sebastien Dryepondt from Oak Ridge National Laboratory for providing us with the PM2000 forged billet used in this study. We would like to acknowledge Dr. Stuart Maloy, Dr. David Hoelzer, and Prof. G. Robert Odette for providing the 14YWT powder (called Batch 1) for this study. The production of the 14YWT powder was funded by the DOE Global Nuclear Energy Partnership program in 2008 subcontract-70553-001-09. Drs, Michael McMurtrey, Xinchang Zhang and Jorgen Rufner are thanked for the execution of the SPS densification of the 14YWT powder. Danny Edwards and Carolyne Burns are thanked for their technical reviews of report sections, and Cary Counts is acknowledged for his editorial review of this report.

Acronyms and Abbreviations

3D	three-dimensional
AM	additive manufacturing
AMMT	Advanced Materials and Manufacturing Technology
ANL	Argonne National Laboratory
BSE	backscattered electron
EBSD	electron backscatter diffraction
EDS	electron dispersive X-ray spectroscopy
FFF	fused-filament fabrication
FIB	focused ion beam
ICP-MS	inductively coupled plasma mass spectrometry
ID	inner diameter
KAM	kernel average misorientation
OD	outer diameter
ODS	oxide dispersion strengthened
PNNL	Pacific Northwest National Laboratory
PSD	particle size distribution
RPM	revolutions per minute
SD	standard deviation
SEI	secondary electron imaging
SEM	scanning electron microscope
SPS	spark plasma sintered
SS	stainless steel
TEM	transmission electron microscopy
XEDS	X-ray energy dispersive spectroscopy

Contents

Figures

Tables

1.0 Introduction

The Advanced Materials and Manufacturing Technologies (AMMT) program develops cross-cutting technologies in support of a broad range of nuclear reactor technologies and maintains U.S. leadership in materials and manufacturing technologies for nuclear energy applications. The overarching vision of the AMMT program is to accelerate the development, qualification, demonstration, and deployment of advanced materials and manufacturing technologies to enable reliable and economical nuclear energy (Li et.al., 2022)

The AMMT program will exploit additive manufacturing (AM) to develop and optimize reactor materials and introduce new high-performance materials into nuclear energy systems. AM is an innovative technique to produce components at near-net shape with minimal machining. In some cases, the typical engineering alloys are not well suited to be produced through AM. Therefore, the AMMT program is further exploring other optimized alloy/manufacturing combinations for improved performance like increased radiation tolerance but also improved high-temperature strength, creep resistance, and environmental effects.

Solid-based AM techniques can overcome some of the challenges in liquid-based AM processes and should therefore be considered in material design and manufacturing as well. Solid-state AM techniques generally are divided into two broad categories—plastic deformation-based and sinter-based—depending on metallurgical bonding mechanisms, range of processible alloys, and resulting microstructures (Tuncer and Bose 2020). Binder jetting uses a binder to hold powder together, followed by sintering that consolidates the powder into a dense part without melting. This technology may be well suited for producing complex parts of oxide dispersion strengthened (ODS) alloys. Other advanced manufacturing techniques use severe deformation to impart high densities of dislocations in the material while forming it into a tube or plate form (Azushima et.al., 2009). This does not allow one to produce complex shapes but can be used to form tube, plate, or rod materials with a high density of sinks for extreme radiation tolerance.

The work presented in this report forms part of a study on solid-based AM techniques of 316 stainless steels (SS) and ODS steel components and supports the vision and goals of the AMMT program relevant to accelerate development and deployment of advanced manufacturing processes. Achieving this can provide a safety improvement through larger safety margins, economic benefit for higher efficiency during operation, and a cost reduction through more effective manufacturing processes and less waste.

1.1 Project Overview

The full work scope of Pacific Northwest National Laboratory's (PNNL's) solid-state manufacturing processes includes studies of developed 316SS and ODS steel sample components to demonstrate the feasibility of three solid-state manufacturing techniques (see Figure 1):

1. Fused-filament fabrication (FFF).
2. Shear-assisted processing and extrusion.
3. Cold spray and friction stir additive manufacturing.

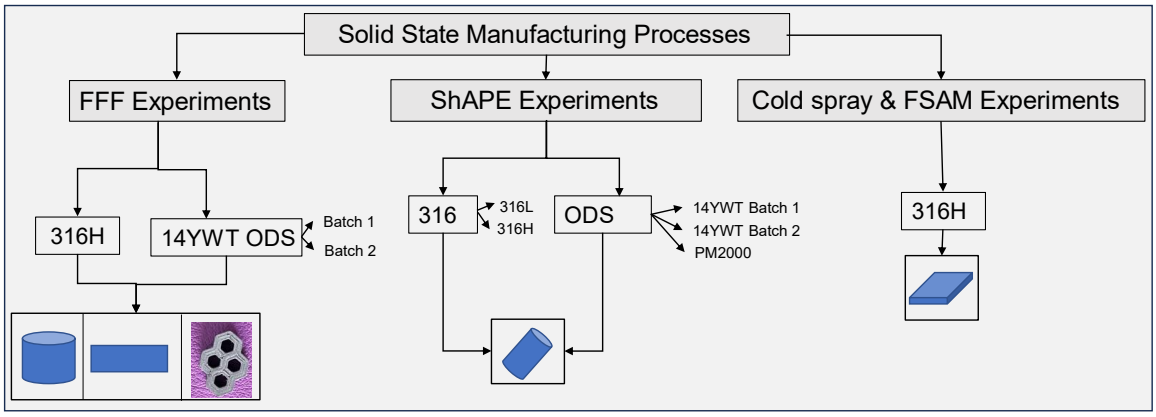

Figure 1. Schematic of the solid-state manufacturing processes feasibility study and process development phases.

The FFF work is already performed and reported by Burns et al., 2023. Although the research and development work of 316H SS using cold spray and friction stir additive manufacturing are already completed ahead of time, it will be presented in a future report.

1.2 Project Objectives

The objectives of the full solid-state manufacturing feasibility project are:

1. Assess the benefits of solid-state advanced manufacturing processes for nuclear energy products. This work will provide feasibility information on alternative routes for ODS steel manufacturing.
2. Demonstrate the sensitivity on final microstructural and residual stresses from the powder microstructure and composition.

This overall project will provide the U.S. Department of Energy (DOE) a critical comparison of three solid-state processes to other AM processes, thereby providing the feasibility of the solid-state processes examined to manufacture 316H SS and ODS steel components.

Specifically for this portion of the project on shear assisted processing and extrusion (ShAPE) tube forming, the objectives will be to determine the feasibility to direct tube forming of high tensile strength steel tubing, specifically for ODS steel to determine the effect of the patented extrusion process on the dispersoids of the ODS material. Additionally, as often ODS powders are mechanically alloyed and therefore more platelike or angular, this feasibility was to explore the impact on the optimization process and initial feasibility of direct tube forming.

1.3 Work Scope

This report provides preliminary information on development of the ShAPE forming for ODS steels only. The work on 316H SS was not performed as first, the feasibility study was performed on the two different ODS types for four experimental trials. Second, the earlier work on 316L SS based on a PNNL Laboratory Directed Research and Development project has only recently been completed on wire ShAPE fabrication only and therefore did not provide sufficient resources and lessons learned to execute the tests as well. The planned work scope for the ShAPE study is shown in Figure 2.

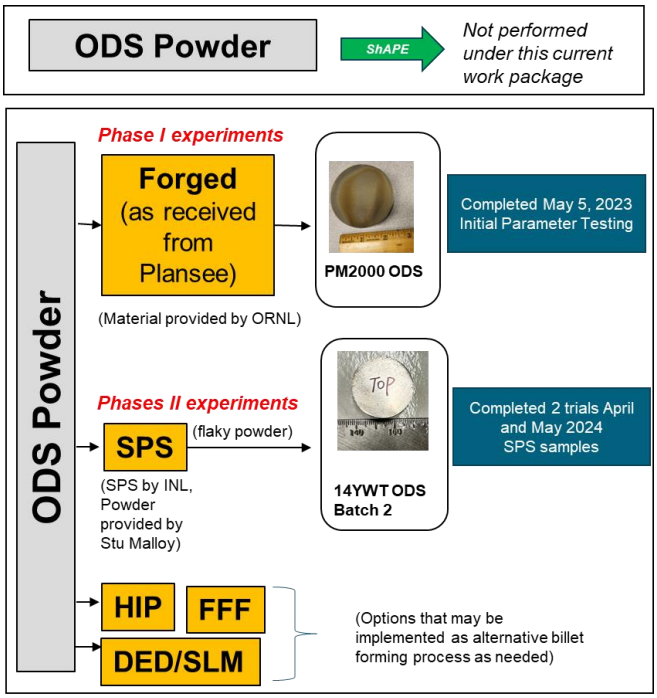

Figure 2. Schematic of the billet forming processes applied for ODS ShAPE experiments.

The preliminary development and characterization of PM2000 extruded tube is described in Section 2.0, while the preliminary development results of 14YWT extruded tubes are described in Section 3.0. The initial feasibility evaluation is presented in Section 4.0.

1.4 Background on ShAPE

ShAPE is a solid phase processing technique that adds an additional shear force compared to conventional extrusion approaches (Figure 3). Significant advantages of ShAPE are that it can be free from feedstock pre-consolidation and preheating, it is more energy-efficient, and it produces products with better strength, ductility, toughness, fatigue life, and surface finish. Research shows improved mechanical properties, fewer processing steps, and lower energy intensity through reduction or elimination of additional thermal processing (Whalen et al., 2021).

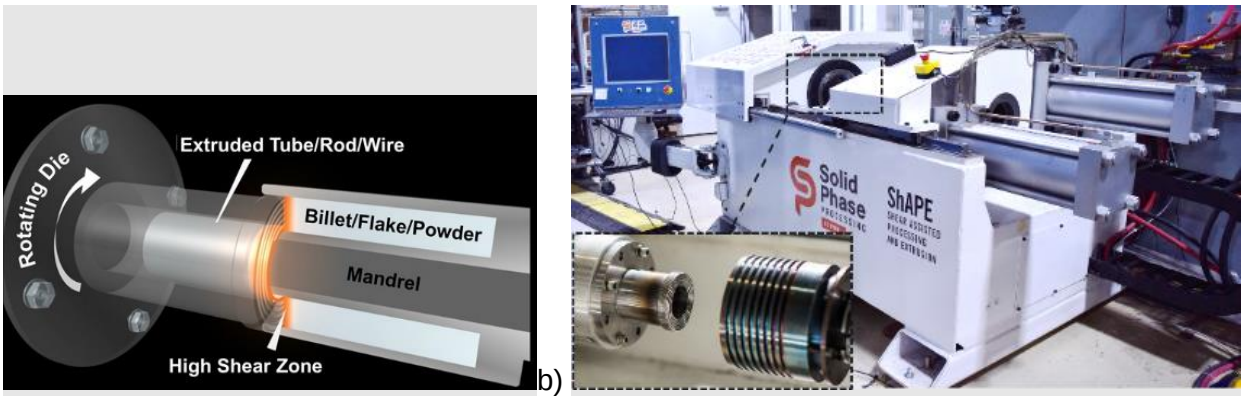

Figure 3. (a) The ShAPE process uses shear to locally heat, consolidate, and extrude materials. (b) The world's first dedicated ShAPE machine at PNNL.

In the ShAPE process, the interaction between the rotating die and the feedstock generates heat and severely deforms the feedstock material resulting in extreme microstructural refinement. Due to severe strain associated with the process, the interface between the clad and the core is metallurgically bonded with the formation of solid solution adjacent to the interface. Overall, extrusions produced via ShAPE (either clad or un-clad) typically exhibit improved performance compared to the conventionally extruded material. With PNNL's current ShAPE machine and direct extrusion tooling, a tube of 12 mm outer diameter (OD) and 0.5 to 1 mm wall thickness and rods of varying diameter can be fabricated from high temperature materials such as steels. With the ShAPE technology, various Al alloys, Mg alloys, copper, nickel, and zircaloy tubes have been successfully fabricated. ODS steel rods also have been fabricated from Incoloy MA956 and CR-166 GARS powders using the ShAPE technology (Zhang et al., 2022). Co-extrusion was successfully demonstrated via the ShAPE process on various alloys systems including co-extrusion of 7075 Al with 1100 Al, pure Cu with pure Ni, and Ni with Zircaloy-4 (Komarasamy et al., 2022).

To withstand the high temperatures and forces that will occur during extrusion, the die materials were carefully chosen and are shown in Figure 4. The key components that experience high temperature and processing forces during ShAPE extrusion are the extrusion die, container, and mandrel. In the current project, these components were designed and fabricated from high temperature materials. For instance, both the die and the mandrel will be made from W-La_2O_3 material. Additionally, the container that holds the feedstock will be fabricated from Inconel 718, a γ″ strengthened nickel base superalloy, which has the necessary high temperature strength, but most importantly it is available in the size ranges that is required and is less expensive than MP159. Overall, the extrusion setup is well considered and designed, and produced tubes from high temperature materials.

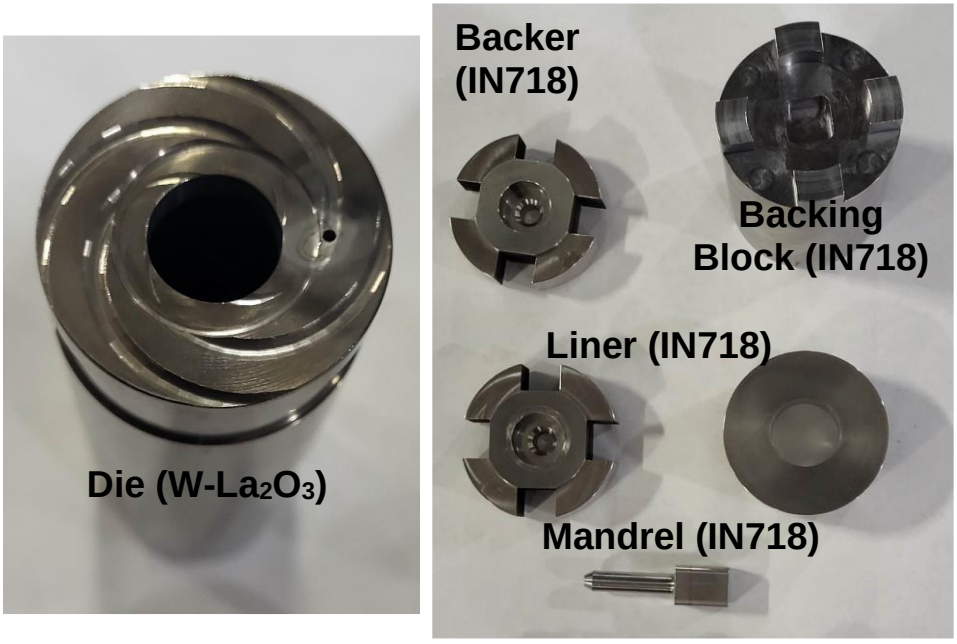

Figure 4. Photographs of extrusion tooling and materials.

2.0 PM2000 ShAPE Manufactured Tube

The research result reported here in this section, was a conference presentation (Silva et.al., 2024a) and a detailed journal publication was submitted to Material Science & Engineering A in September 2024b. (Silva et.al., 2024).

2.1 Material and Technique Description

The starting material for this work was a 64 mm diameter rod of ODS PM2000 alloy (Fe20Cr5Al) in its uncrystallized (or unannealed) form was purchased from Plansee USA LLC and provided by Sebastien Dryepondt from ORNL. PM2000 alloy consisted of 74.12, 19.13, 5.46, 0.48, and 0.39 wt.% of Fe, Cr, Al, Ti, and Y as the major elements, respectively, with 0.02 wt.% Si. It also contained C, N, O, and S at 14, 86, 2480, and 8 wppm, respectively. PM2000 (a ferritic alloy) was developed to have high mechanical strength, improved radiation tolerance and oxidation resistance compared to conventional Fe-Cr alloys. Alloy composition with high Cr can form radiation-induced Cr-rich α′ precipitates, which have embrittling characteristics at certain temperatures (~475°C) (Capdevielle et al., 2010). The addition of Al helps lowering the formation of Cr-rich α′ phase precipitates and thereby radiation-induced embrittlement of the material (Field, et al., 2015., Briggs, et al., 2017). The increased oxidation resistance of PM2000 is due to the formation of protective oxide layers such as Cr_2O_3 and Al_2O_3, however, it can be reduced if the Al concentration reduces below a critical value (Dryepondt et al., 2013, Dryepondt et al., 2018., Marechal, et al., 2003).

Figure 5 provides the process input such as die rotational speed (revolutions per minute [RPM]) and ram speed. The rotational speed and velocity were 430 RPM and 5.0 mm/min, respectively during the processing step. The total die plunge depth was about 9.6 mm in which 8.8 mm was part of the steady-state processing with respect to the processing parameter input. The extruded tube was subjected to various characterization as discussed in the next subsections.

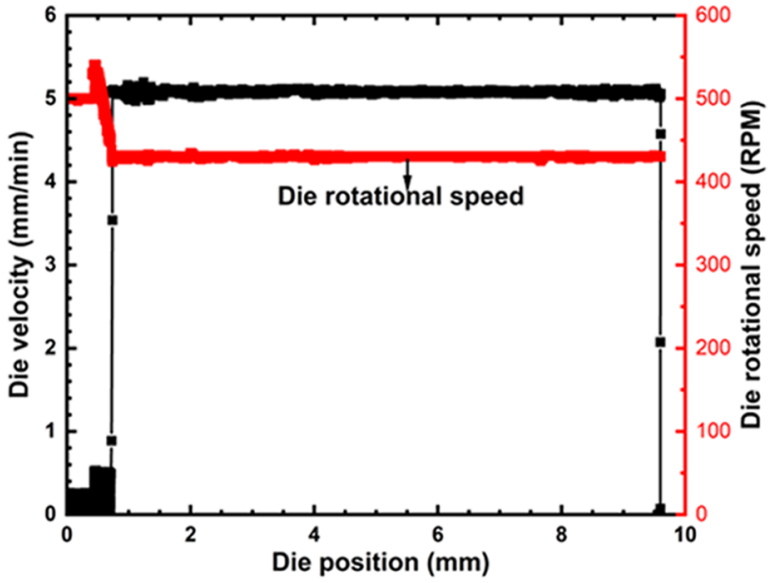

Figure 5. Process input parameters along the die position used in the process.

2.2 Characterization Techniques

Powder X-ray diffraction (XRD): A Bruker D8 Discover TXS-HE A25, equipped with a rotating Cu anode (Kα λ = 1.54060 Å), 0.3 x 3 mm cassette tungsten filament, Atlas goniometer, and a UMC 1516 motorized xyzϕχ stage, was used to collect XRD patterns of the base metal longitudinal section and the extruded tube in both transverse and longitudinal sections at the middle of the extrudate. Samples were positioned using a laser-video alignment system. The power settings of the generator were 45 kV and 120 mA and the source-sample distance was fixed at 425 mm. More details of the samples will be noted in the sections where data are provided. This instrument was equipped with a Dectris EIGER2 R 500K area detector allowing the collection of high intensity data in a smaller time. Therefore, a step size of 0.005° and a 0.05 sec/step time with a focusing Goebel mirror configuration and 2 mm collimator were used in collecting the XRD patterns over 30–105° 2θ range. These XRD patterns were fitted using Rietveld refinement using GSAS software.

Scanning electron microscopy (SEM): A JEOL 7600F SEM was used for imaging in secondary electron (SE) and back scattered electron (BSE) modes, energy dispersive spectroscopic (EDS) elemental mapping, and electron backscatter diffraction (EBSD) scans. A 20 kV voltage and 16 high current mode with an aperture size of 1 and a step size of 130 nm were used for EBSD scans, while varied voltages up to 20 kV were used the SEM imaging and EDS elemental maps acquisition. EBSD data analysis was performed in MTEX 5.6.1 using MATLAB R2019b. The ferritic phase was indexed using an iron bcc crystal structure with a 2.866 Å lattice parameter. Indexing hit rates varied from sample to sample and ranged between 75-96% depending on the grain size. Since both magnification (1,000x) and step size (130 nm) were kept constant, a standard data treatment recipe was applied for all datasets. Data denoising was performed using a 5-pixel neighbor de-noise protocol, followed by mild softening using a half quadratic filter with alpha and EPS values of 0.01. Low-angle grain boundary reconstruction was performed within a misorientation range of 2–15°, whereas high-angle grain boundaries were reconstructed for misorientations ≥15°. Kernel average misorientation (KAM) was used after careful data denoising [3] to identify dense dislocation walls forming within grains for misorientation angles lower than 3°.

Transmission electron microscopy (TEM): A JEOL Grand Arm Scanning TEM (STEM) was used to collected STEM images and X-ray energy dispersive spectroscopy (XEDS) elemental maps of the samples. The GrandARM is equipped with a dual Centurio energy dispersive spectrometer, with each silicon drift detector having a collection area of 0.98 sR per detector. The STEM is equipped with a Schottky field emission gun that can be operated at 300 keV voltage. STEM imaging was performed using both bright field (BF) and high-angular dark-field (HAADF) modes. Lamella of the samples for STEM imaging were prepared using either a FEI Quanta FEG or a Helios Hydra Plasma focused ion beam at 30 kV accelerating voltage and 100 pA–4 nA currents. The lift-out was then thinned to electron transparency using the Quanta Ga-FIB at varying kilovolt and current levels. The initial steps involved thinning at 30kV 30 pA–3 nA currents followed by 5 kV, 50 pA, and final clean-up at 2 kV, 20 pA.

Microhardness testing: Vickers microhardness testing was performed on epoxy-mounted and polished samples (0.08-µm finish) using a CM-802AT microhardness tester (Sun-Tec Corporation) per ASTM E384, 2022. A calibration block was used periodically to verify operation of the tester. Vickers microhardness testing was performed using a 300-gf load and dwell time of 15 s. For each specimen, at least 50 indents were made, and the average was calculated. All microhardness data were obtained at same locations where SEM and TEM data were collected for consistency.

2.3 ShAPE-Extruded ODS PM2000 Tube

A photograph of the extruded tube and its cross section are presented in Figure 6 and Figure 6b. As noted in Figure 6(c), the die temperature was around 1,250°C at about 2 mm plunge position. The temperature rise is due to frictional and adiabatic heating of the tooling and the billet material. The spindle torque was below 150 Nm and the ram force was below 40 kN for most of the extrusion. The rise at the end is due to the end of the billet and the supposed deformation volume is interacting with the container base that is not deforming and is not at the billet steady-state temperature. Overall, the forces and torque were lower than expected, hence the processing temperature can be reduced further to below 1,000°C to preserve the density of oxide dispersions for future similar material processing and optimization. After the processing, it was noted that the Inconel 718 mandrel had broken off during the extrusion process. The die failure can be mitigated by reducing the processing temperature and time, cooling the mandrel, and/or using W-based mandrel material.

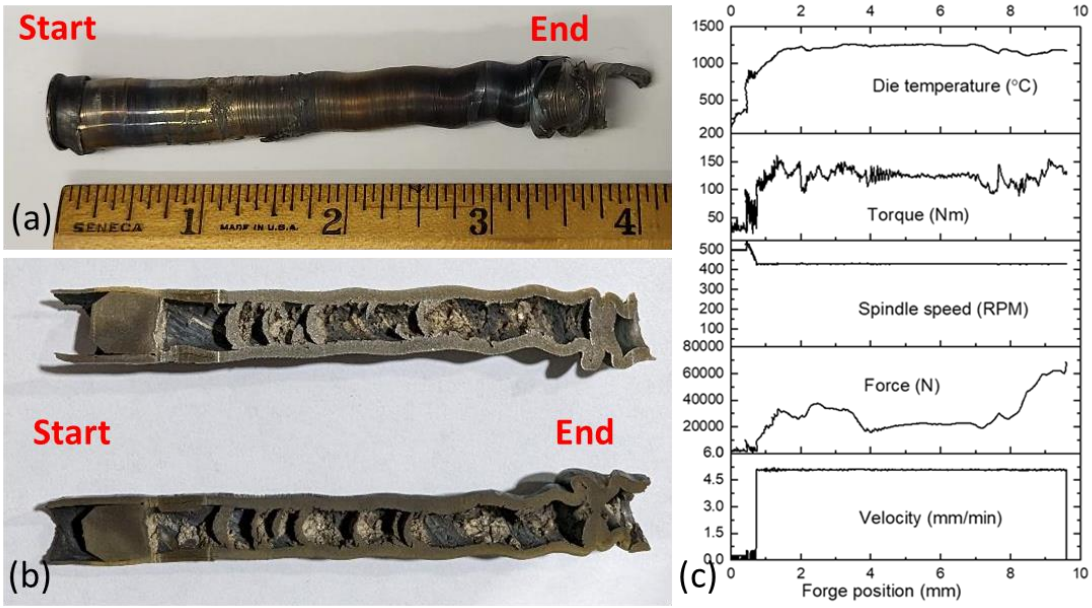

Figure 6. Image showing (a) the PM2000 tube extruded via the ShAPE process, (b) its cross section showing that the extrudate is a tube for the most part, and (3) vertical indirect extrusion process output.

2.4 Crystallographic Data of As-Received and ShAPE-Extruded PM2000 Samples.

XRD patterns of PM2000 base metal were collected on the longitudinal side as shown in Figure 7a. In the case of PM2000 ShAPE extrudate, XRD patterns were collected along both longitudinal and transverse directions. The longitudinally cut section of PM2000 ShAPE extrudate at its middle area is shown in Figure 7b. A sample cut from the PM2000-ShAPE extrudate near its middle area to represent the transverse direction (Figure 7c) of the extrudate was used to collect both average XRD pattern and micro-XRD patterns (10 scans). Figure 7 also shows the sample used for micro-XRD scans at three different spots for example (Figure 7d-f). These scans were performed across the sample with ~5 mm distance from each scan.

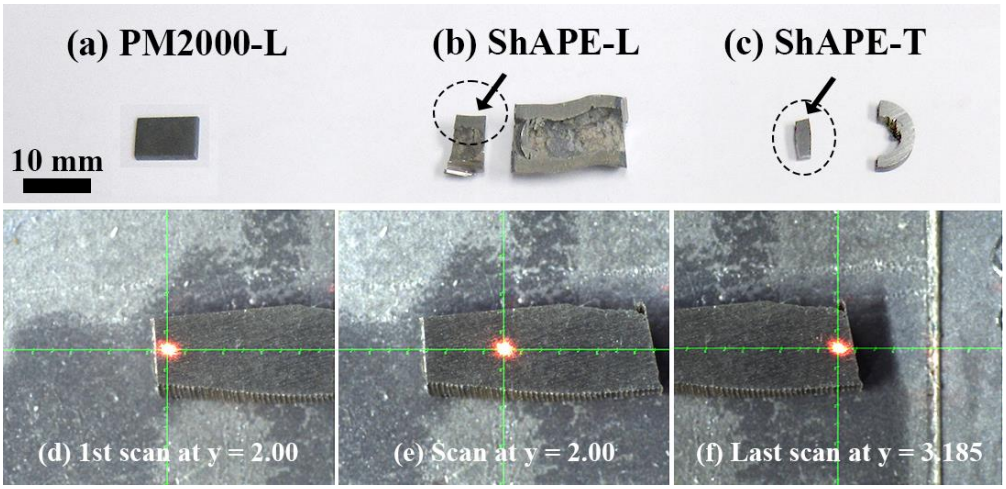

Figure 7. Details for XRD scans. (a) PM2000 base metal cut along longitudinal direction, (b) ShAPE extruded PM2000 sample along longitudinal direction, (c) ShAPE extruded PM2000 sample cut along transverse direction, and (d–f) images of the transverse cut PM2000 ShAPE extrudate sample showing typical spot scans used for micro-XRD pattern acquisition. (L: longitudinal; T: transverse directions).

XRD patterns of as-received (base metal PM2000) and ShAPE extruded (near the tube center) PM2000 samples (Figure 8a-b) showed only the presence of Fe-based body-centered cubic (bcc) ferritic structure with a space group of Im-3m. Rietveld refinement showed a smaller lattice parameter of the ShAPE samples compared to the as-received PM2000 alloy, but the decrease was only 0.04 to 0.07 % Figure 8, which is insignificant. This slight change in the lattice parameter is also observed in the peak shift highlighted in Figure 8b. Rietveld refinement further showed the as-received PM2000 alloy sample to have preferred orientations parallel to {200} and {211} planes of the bcc structure. These preferred orientations are not observed in the ShAPE samples. Rietveld analyzed XRD patterns of each sample are shown in Appendix A. Micro-XRD patterns (Appendix A) collected on the ShAPE transverse cut from the middle of the extrudate showed no significant change in peak positions suggesting no significant crystallographic changes locally in the extrudate.

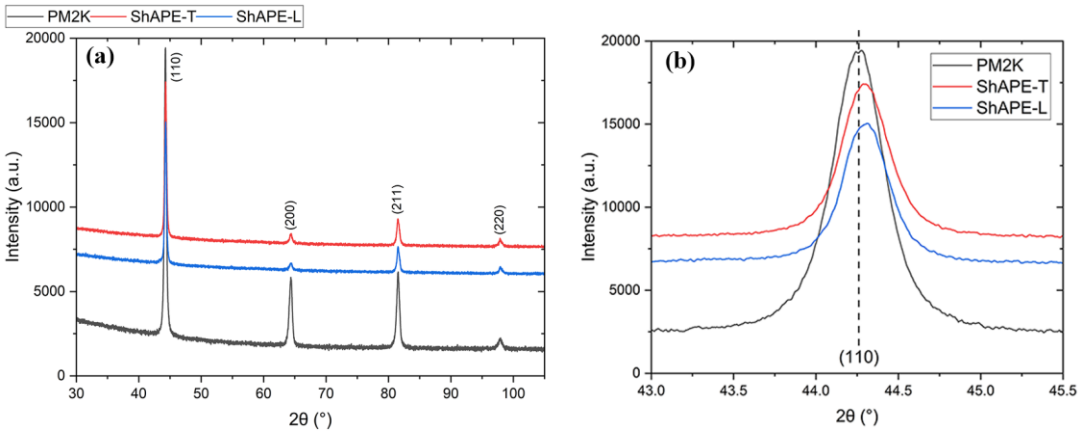

Figure 8. Powder XRD patterns of PM2000 (as-received and ShAPE) samples using (a) full scanned range and (b) (110) Bragg reflection with a dotted line indicating the approximate center of the peak for PM2000 sample. ShAPE-T and -L denote samples cut along transverse and longitudinal directions, respectively.

Table 1. Crystallographic properties of PM2000 (as-received rod and ShAPE tube near its center) samples. Goodness of the Rietveld refinement of all XRD patterns is ~0.8%. Lattice parameter (LP) decrease in the SHAPE samples are correspond to the LP of PM2000 as-received sample. P.O. represents preferred orientation(s).

Sample	L.P. (Å)	σ (Å)	Decrease (%)	P.O.
PM2000	2.8923	0.0001	N/A	(200), (211)
ShAPE-T	2.8912	0.0001	0.04	None
ShAPE-L	2.8904	0.0001	0.07	None

2.5 Microscopic Data of As-Received and ShAPE Extruded PM2000 Samples

2.5.1 SEM Examination

Typical SEM micrographs of the as-received PM2000 material along transverse and longitudinal directions are presented in Figure 9. The as-received material consists of equiaxed grains (Figure 9a) with some secondary precipitates/particles of varied size. SEM micrograph of the sample along the longitudinal direction (Figure 9b) shows preferred oriented and elongated grains along the rod's rolling direction. These two observations indicate the material to be equiaxed in the transverse orientation but elongated in the longitudinal orientation. The secondary precipitates/particles that can be observed in dark-contrast areas in the BSE images are present throughout the sample (Figure 9b-e). Some of these secondary precipitates are large (>100 nm) and some are at nanoscale (Figure 9d; ~20 nm) resulting in a range of precipitate size (~20–230 nm). The elemental maps also suggest these secondary large particles are rich with aluminum (Al). Data obtained from further analysis of these large and small precipitates at high-resolution using STEM will be discussed later in the text (Section 2.5.3).

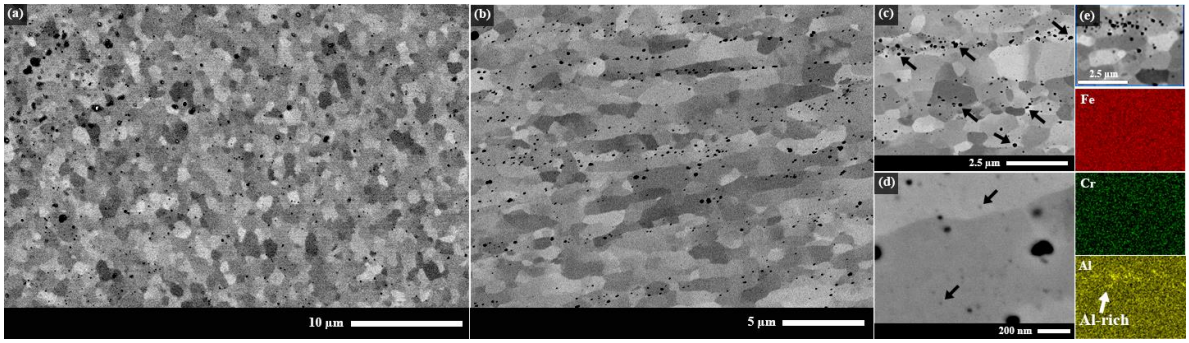

Figure 9. BSE SEM micrographs of PM2000 as-received rod samples cut along (a) transverse and (b) longitudinal directions. (c – e) BSE SEM images of longitudinal sample at two different resolutions. Fe, Cr, and Al elemental maps of the sample area depicted in (e) are also shown.

While SEM scanning was performed on the general region of ROI1 (Figure 10) of the start section of the extrudate, images have been collected to cover the crack area and three regions of the sample covering top (1), middle (2), and lower (3) areas of the start section as depicted in Figure 10.

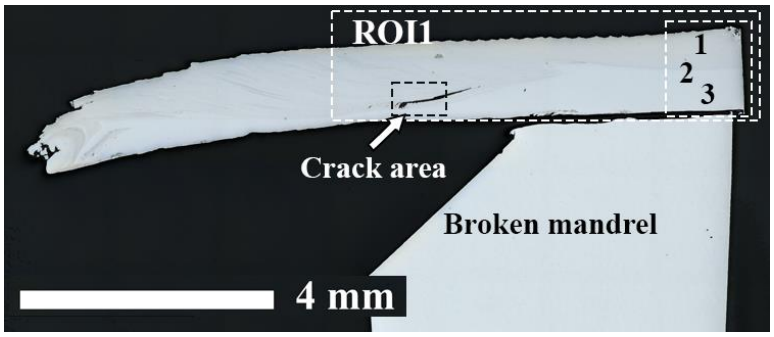

Figure 10. Optical micrograph showing the general area of interest (ROI1) and other regions (crack area and regions 1, 2, and 3) of start location of longitudinally cut ShAPE extrudate sample used for SEM scanning.

A few areas of the extruded PM2000 tube surface (longitudinal direction) consisted of cracks, and one such crack areas observed at the start of the tube is highlighted in Figure 11a. These cracks/openings are also consistent with extrusion-induced interfaces or mass flow lines corresponding to the material flow direction observed in that sample area (Figure 11a). This observation suggests crack formation and propagation along these mass flow lines. Microstructure of the sample in the vicinity of the crack also consists of significant amount of porosity both at micro- and nano- scales Figure 11b-c. The bright-contrast metal carbide precipitates are also present in this region. This precipitation propagates into the tube, especially in the outer surface of the tube (Figure 11d). As confirmed using EDS elemental maps of one such areas (Figure 11e), these bright-contrast precipitates are carbides rich with Cr and W, suggesting the carbide formation is coming from the ShAPE induced friction of the base metal and the tools utilized in the tube extrusion process. The inner part of the start of the tube (Figure 11f) is free of these secondary metallic carbide precipitates at significant level. However, dark-contrast precipitates as were observed in the PM2000 base metal can be observed in the inner part of the extruded tube (Figure 11g). More SEM micrographs of these areas can be found in Appendix B. Similar to the start section of the PM2000 tube (longitudinal direction), the middle (Figure 12) section of the ShAPE extrudate, especially in the outer diameter surface, also has metallic carbide precipitates due to friction-induced reaction between the extruded tube surface and the tools used in the ShAPE.

Figure 13a shows of an optical micrograph of the end section of the longitudinally cut sample of ShAPE extrudate at its end section. In this end section, three regions were further scanned using BSE SEM imaging. As depicted in Figure 13b, outer region of the area contained some microcracking and the bright-contrast precipitates as in the other sample areas. The microstructure close to the middle region of this end section mostly consist of dark-contrast precipitates (Figure 13c-d). Other than these features, inner diameter region of the end section of the sample also showed to contain bulky square precipitates (Figure 13e-f). EDS elemental mapping using SEM at this resolution could not determine what these precipitates are as shown in Appendix B. Therefore, further analysis of these nano-precipitates was done using high-resolution STEM and XEDS elemental mapping and will be discussed below.

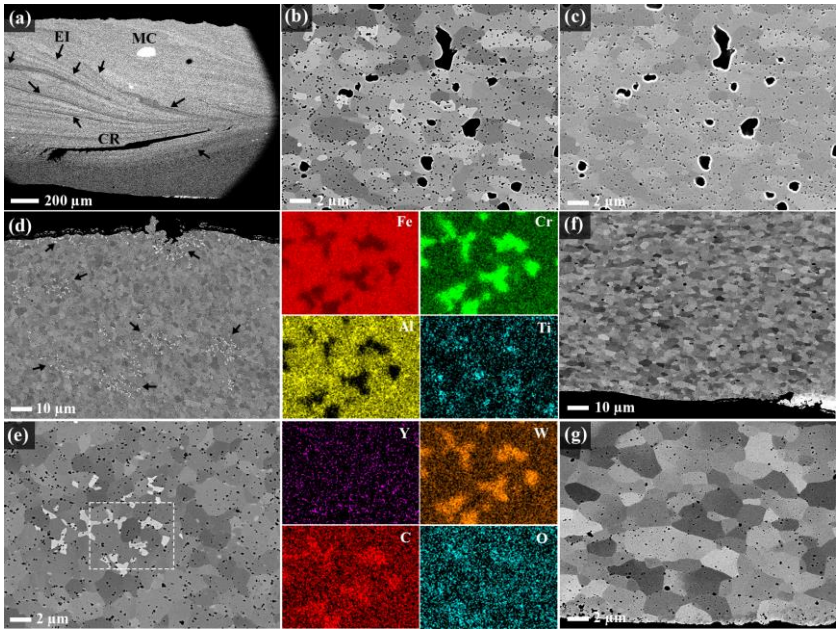

Figure 11. SEM micrographs of longitudinally cut ShAPE extruded tube sample near start section. BSE SEM image near the middle of tube surface at (a) low and (b) high resolution. (c) SE SEM image of (b). BSE SEM images of (d-e) the outer and (f-g) inner areas of the tube surface at different resolutions. Elemental maps acquired focusing on the area highlighted in (e). EI, MC, and CR denote extrusion-induced interfaces, metal carbides, and cracks, respectively.

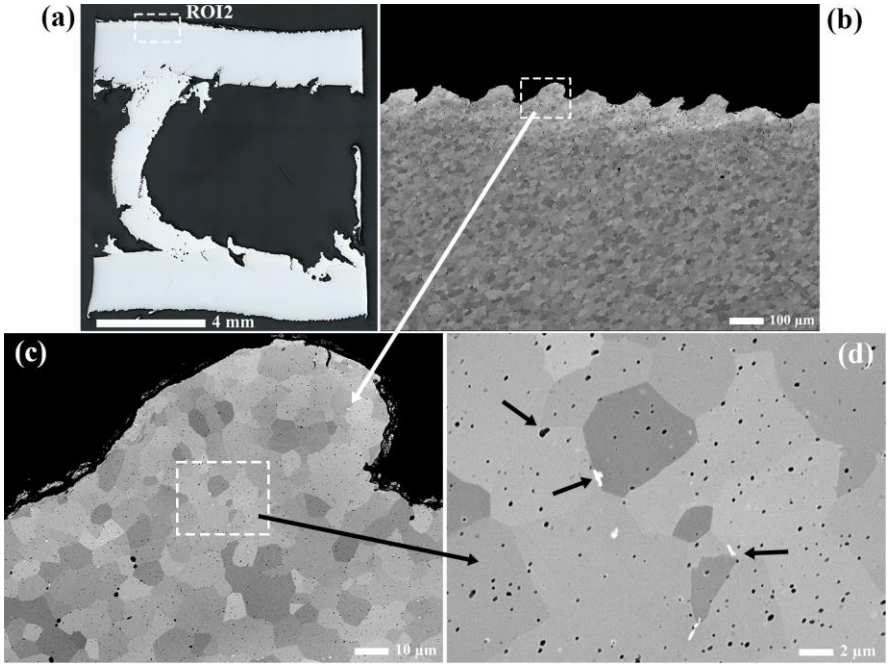

Figure 12. (a) Optical micrograph and (b) the BSE SEM image of the middle section of ShAPE extrudate along the longitudinal direction showing the area scanned (ROI2). (c-d) An area at two different high-resolutions showing bright-contrast and dark-contrast precipitates in the sample area.

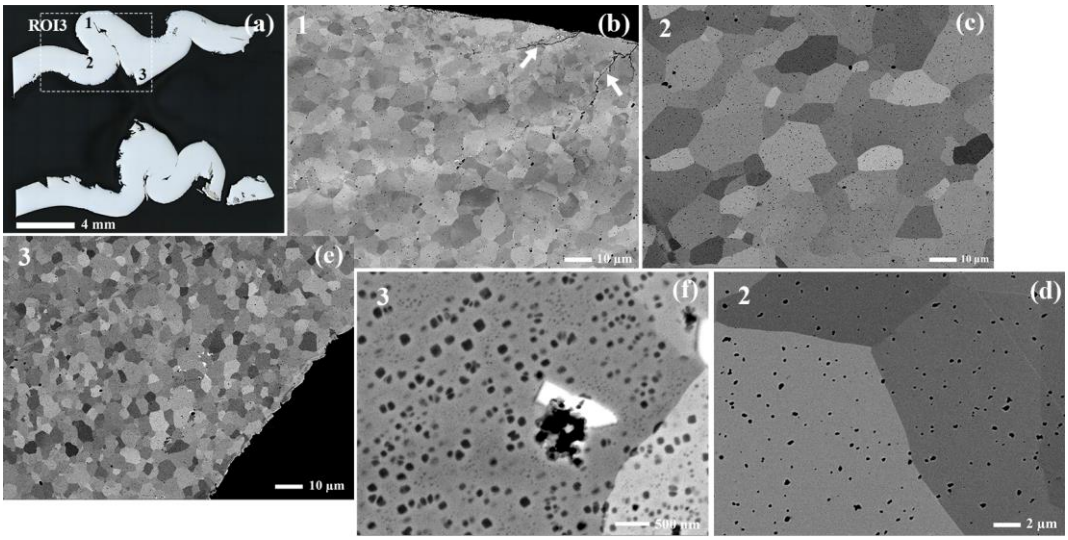

Figure 13. (a) Optical micrograph showing the areas scanned to collect SEM images in the end section of ShAPE extruded longitudinally cut sample. BSE SEM micrographs of (b) region 1, (c–d) region 2, and (e–f) region 3.

A sample of the PM2000 ShAPE extrudate was also cut near the middle section of the tube and was mounted in epoxy so that the cross-section or its transverse direction can be analyzed. SEM, EBSD, and microhardness data were collected at the center of this sample as highlighted in Figure 14. As in some of the other cases, inner and outer diameter of the tubing in this area of the sample was selected to acquire SEM and EBSD data.

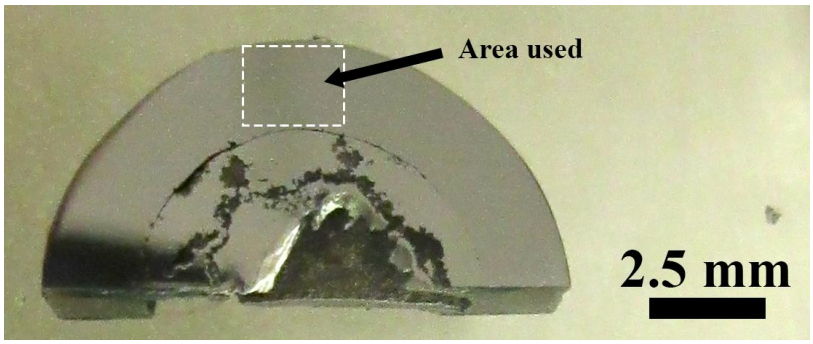

Figure 14. Photograph of the transverse cut of ShAPE extrudate used for further characterization. The area highlighted by a rectangle used for the analysis.

SEM imaging showed the presence of mostly equiaxed grains in the ShAPE extruded tube of PM2000 sample cut along the transverse direction near the tube's center (Figure 15a-c). Both inner and outer diameter regions of the tube consist of this equiaxed grain structure. This sample also contained dark-contrast precipitates. EDS elemental maps of the bulk sample area in the outer diameter region (Figure 15c) show these precipitates to be Al and Y-rich oxide phase, while Ti-rich precipitate areas are also observed. Inner diameter region also showed similar elemental distribution as shown in Appendix B. High-resolution elemental mapping confirmed the presence of (Al, Y)Ox phase as depicted by the second set of EDS maps in Figure 15.

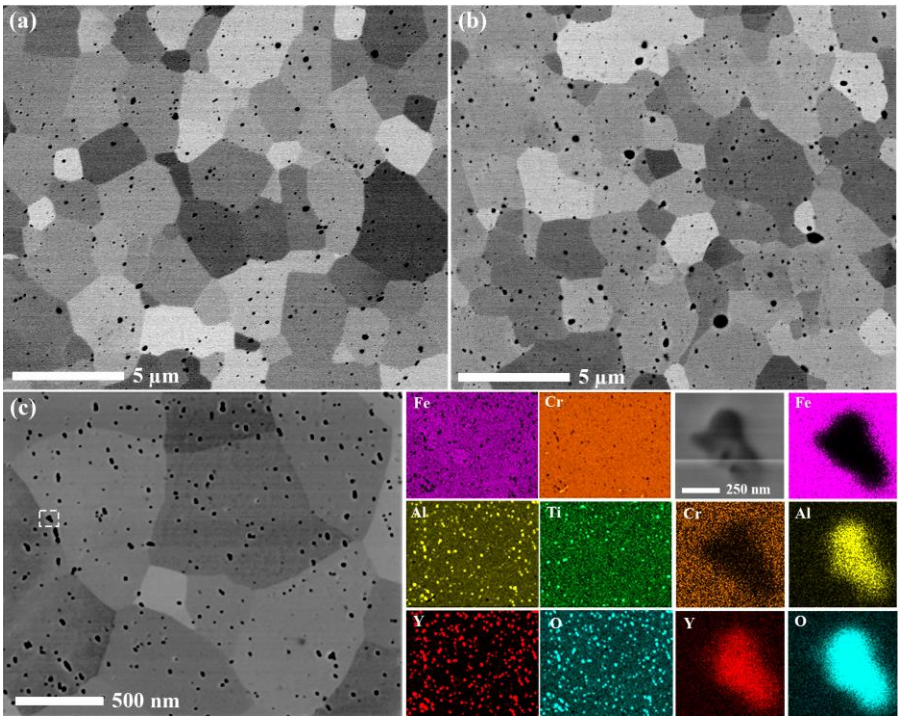

Figure 15. BSE SEM images of (a-b) inner and (c) outer regions of a sample cut along transverse direction of the extruded PM2000 tube near its center. First and second sets of elemental maps are for the whole area shown in (c) and the particle area highlighted in (c).

2.5.2 EBSD Results

As was observed using SEM imaging, EBSD inverse pole figures also showed the PM2000 base metal sample cut along the longitudinal direction to consist of an elongated grain structure parallel to the rod's rolling direction (Figure 16a), while the sample cut along the transverse direction has an equiaxed grain structure (Figure 16c). Qualitative measurements of KAMs of the two samples (Figure 16b and d) do not show significant strain in the sample area analyzed.

The ShAPE extrudate at its start location and its outer diameter region (Figure 17a) mainly showed to contain equiaxed grain structure as shown in Figure 17b and c. Slight strain is observed along some grain boundaries in the KAM map (Figure 17d).

Middle and end sections of the PM2000-ShAPE extrudate sample cut along the longitudinal and transverse directions were also characterized using EBSD. In these three sections, both inner and middle diameter regions were used for the scanning. Figure 18a and Figure 18c show these regions of the middle and end sections of the extrudate cut along the longitudinal direction, while Figure 18b shows the transverse cut sample used for the EBSD scanning.

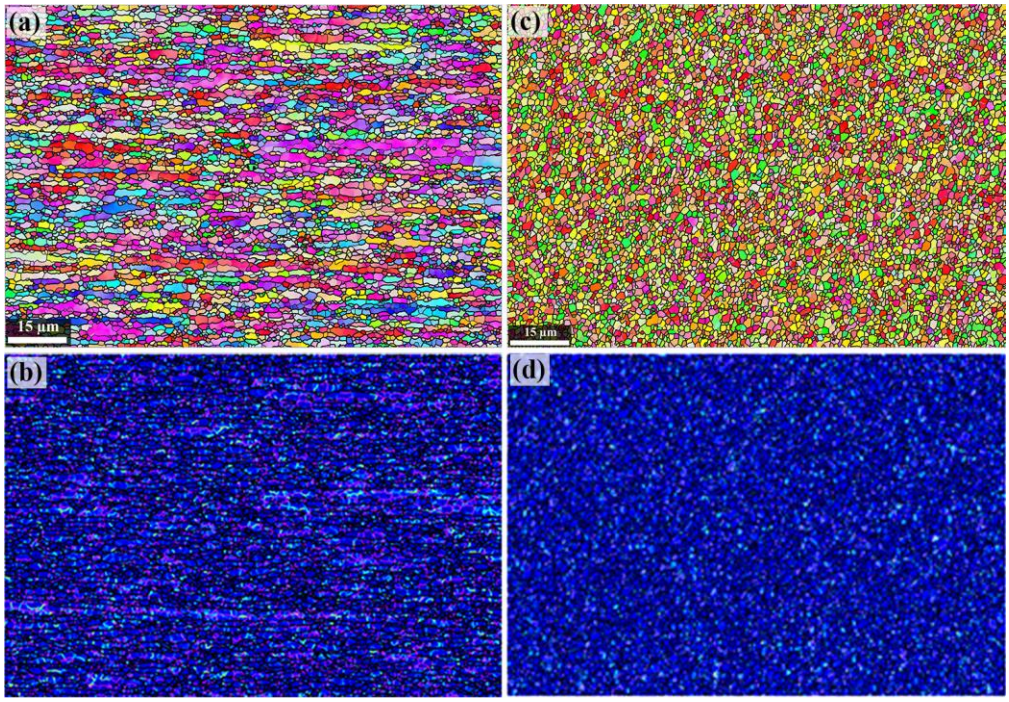

Figure 16. (a) EBSD z-direction orientation map (OM) and (b) kernel average misorientation (KAM) map of PM2000 base metal along longitudinal direction. The (c) orientation map and (d) KAM map of base metal PM2000 along its transverse direction.

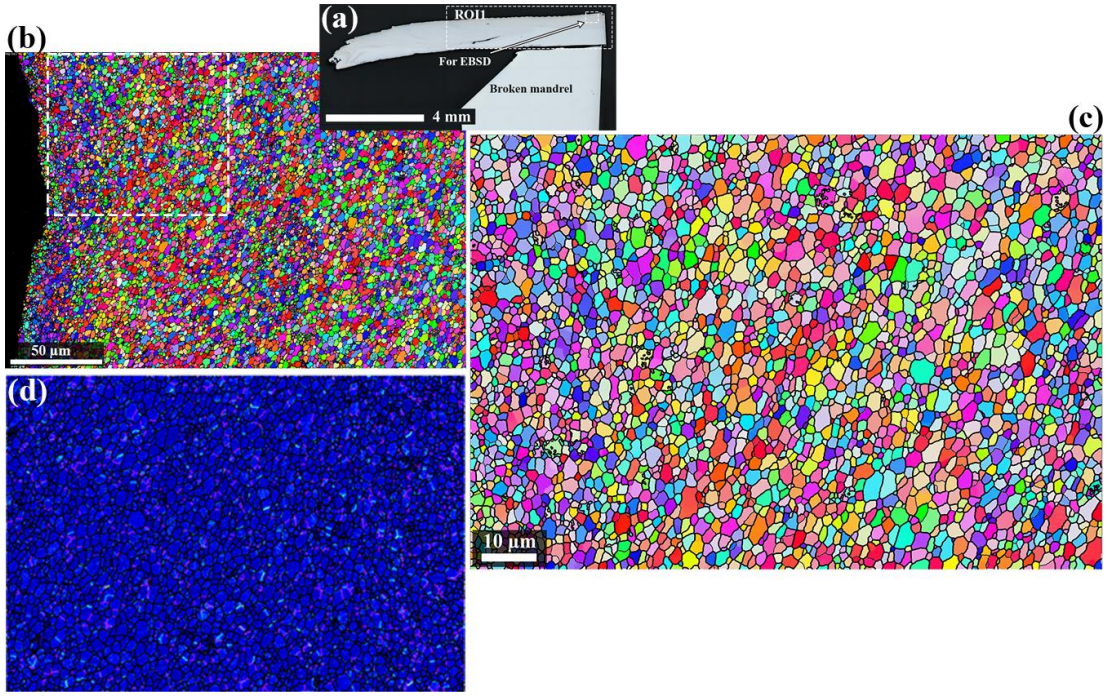

Figure 17. (a) Optical image of the longitudinally cut start section of the ShAPE extrudate highlighting the outer diameter area focused for EBSD scans: EBSD z-direction orientation map of (b) the full area and (c) the area highlighted in (b) and the corresponding (d) KAM map.

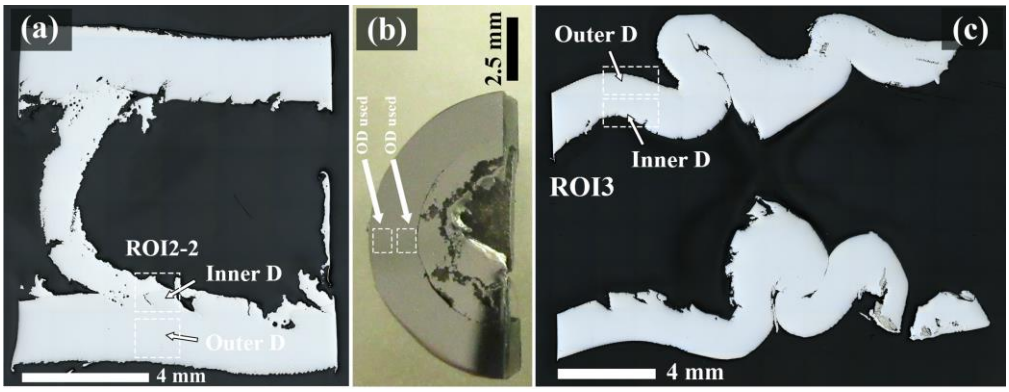

Figure 18. (a) Optical image of the longitudinally cut middle section, (b) photograph of transversely cut middle section, and (c) longitudinally cut end section of the ShAPE extrudate highlighting the inner and outer diameter regions focused for EBSD scans.

An equiaxed grain structure was observed in the ShAPE extrudate at its middle section both along the longitudinal and transverse directions, while larger grain sizes are observed in the outer regions of both samples compared to that of the inner regions. The equiaxed grain structure and the grain size difference can be observed in the orientation maps depicted in Figure 19a, c, e, and g. Both these samples show only minor strain along some grain boundaries according to the KAM maps of inner and outer regions shown in Figure 19b, d, f, and h. This observation is somewhat like the base metal and the ShAPE star sections and will be discussed in detail using quantitative data in the discussion section.

The end section of the longitudinally cut ShAPE extrudate sample also showed similar behavior to that of ShAPE extrudate's middle section. That is, the inner region of the end section (Figure 20a) shows to container smaller grains compared to that of the outer diameter region (Figure 20b). KAM maps also show closely similar strain distribution to that of other samples. However, more quantitative data will be discussed later in the text.

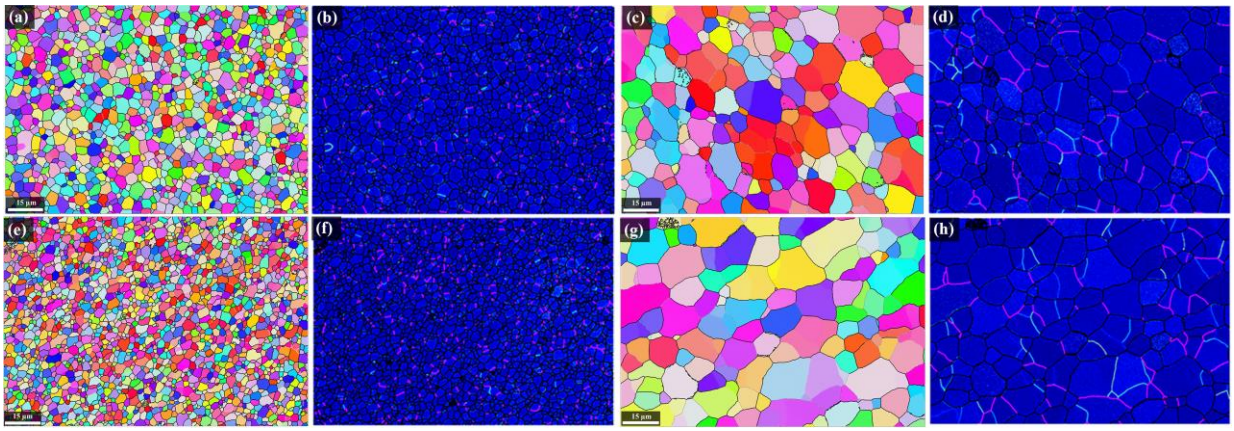

Figure 19. EBSD data of the longitudinal and transverse cut ShAPE extrudate at their middle section. (a) OM, (b) KAM map of middle section at the inner diameter region and the outer diameter regions in (c) and (d). For the transverse cut middle section samples, (e), (f) and (g), (h) represent the inner diameter and outer diameter images, respectively.

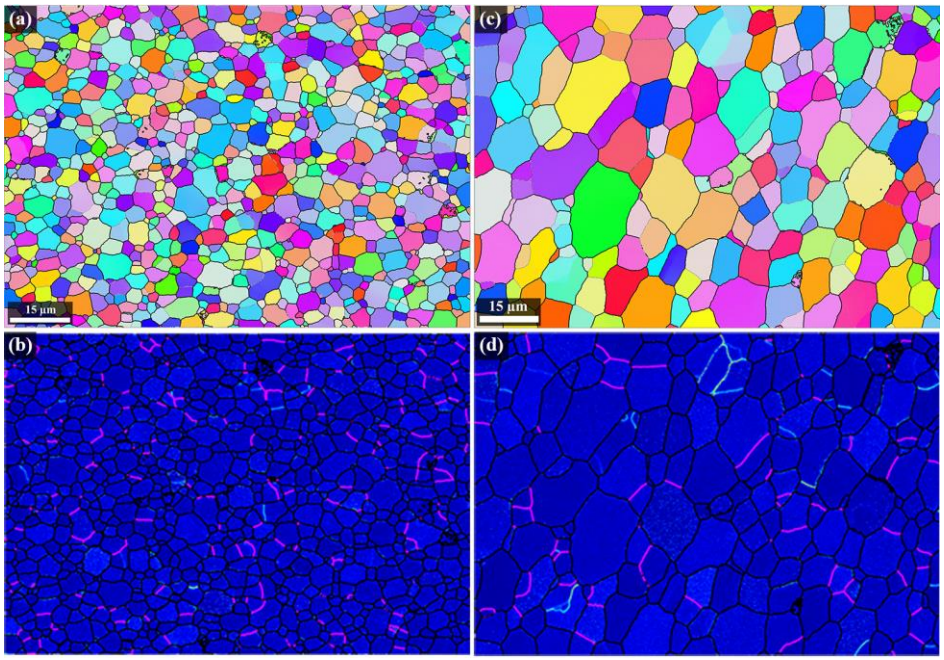

Figure 20. EBSD data of the longitudinally cut end section of the ShAPE extrudate. (a) OM and (b) KAM map of the end section at its inner diameter region. (c) OM and (d) KAM map represent the outer diameter region images.

As is shown in Figure 21a-b, the grain area of base metal PM2000 is lower than the ShAPE extruded tube samples both along longitudinal and transverse directions. Also, the grain area increase can be observed in the order of base metal to start to middle/end of the extruded tube (Figure 21a). The grain size distribution of the middle and end sections of the tube do not have a significant difference, while only slight grain area increase is observed in the start section of the ShAPE extrudate compared to the base metal sample. In the case of cross sections (transverse direction) of the ShAPE extruded tube, grain sizes of both inner and outer diameter areas are larger than that of the base metal sample (Figure 21b). Also, a greater percentage of larger grains can be observed in the outer diameter than the inner diameter of the ShAPE extruded tube sample. These observations suggest a grain growth in ShAPE extruded tube due to the ShAPE-induced grain growth or recrystallization with lowest grain growth effect on the inner part of the extrudate as is observed in other reported studies carried out using ShAPE (Overman et al., 2017).

The distribution of misorientation angles of PM2000 base metal and outer diameter of start section of the extrudate are similar (Figure 21c), suggesting no significant change in the microstructure of the start section of the extrudate. In the outer diameter of middle section of the extrudate, only slight increase in low and high angles than the base metal and the start section of the extrudate can be observed. A similar observation can be made in the case of grain boundaries of the end section of extrudate compared to the base metal. The closely similar grain boundary distributions, which vary within the statistical deviation from one sample to another, indicate consistent microstructures in the base metal and ShAPE extrudate of PM2000. Similar characteristics can be observed in the cross section of the base metal and inner diameter area of the cross section of ShAPE extruded samples (Figure 21d), while outer diameter area of the cross section of extrudate (Figure 21d) shows similar misorientation angle distribution to that of the outer diameter middle section of the extrudate (Figure 21c).

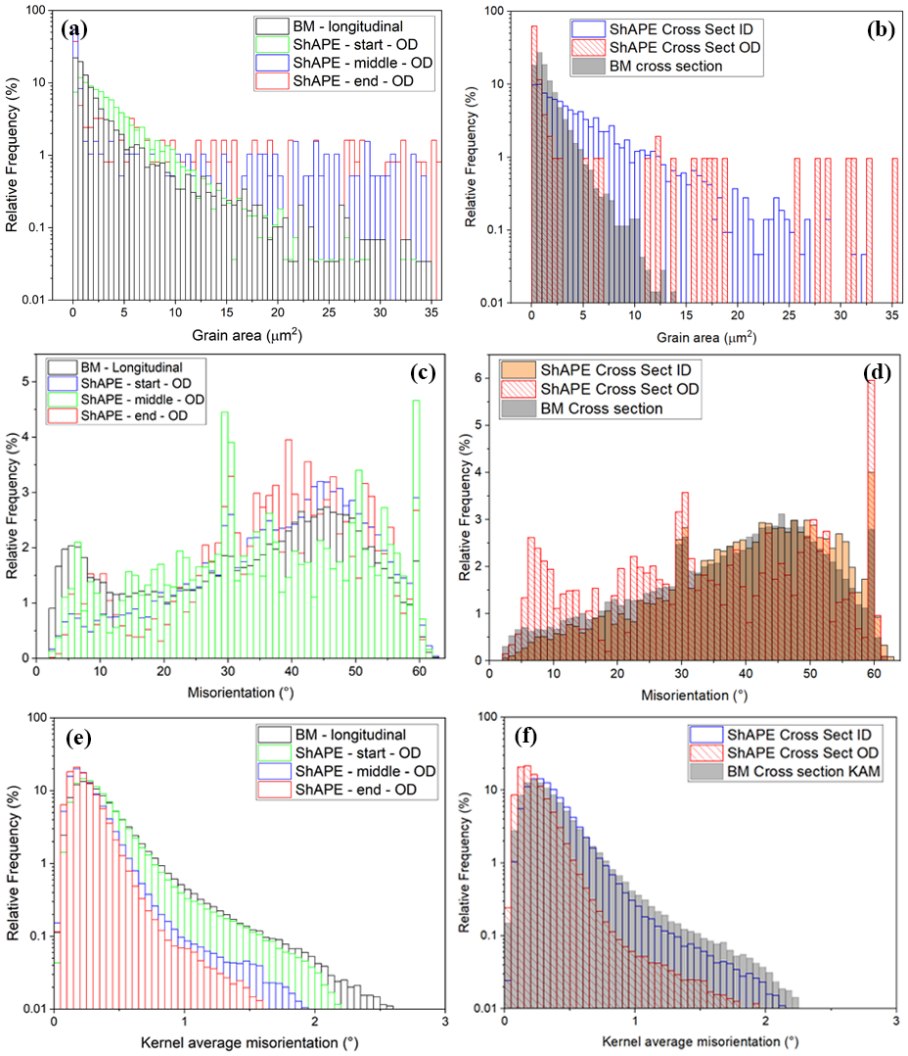

Figure 21. Grain area, misorientation angles, and KAM distribution of PM2000 base metal rod compared with the ShAPE extrudate along longitudinal and transverse (cross section) directions. (a-b) Grain area, (c-d) misorientation angle, and (e-f) KAM comparisons. Inner diameter (ID) and OD denote inner diameter and outer diameters of the extrudate, respectively. Note that only the middle section of the extrudate representing the ShAPE was used for transverse direction analysis.

KAM maps of the samples also indicate a decrease in the relative frequency of kernel average misorientation angles from base metal to start to middle to end sections of the ShAPE extruded tube (Figure 21e-f). Such decrease in KAM angles corresponds to a decrease in strain, suggesting intra-granular relaxation as a result of the grain growth/recrystallization, especially at outer diameter, during ShAPE extrusion of PM2000.

2.5.3 TEM Evaluation

STEM imaging showed the presence of clusters of line dislocations and nano-sized precipitates as can be observed in Figure 22a-d in the base metal PM2000 sample.

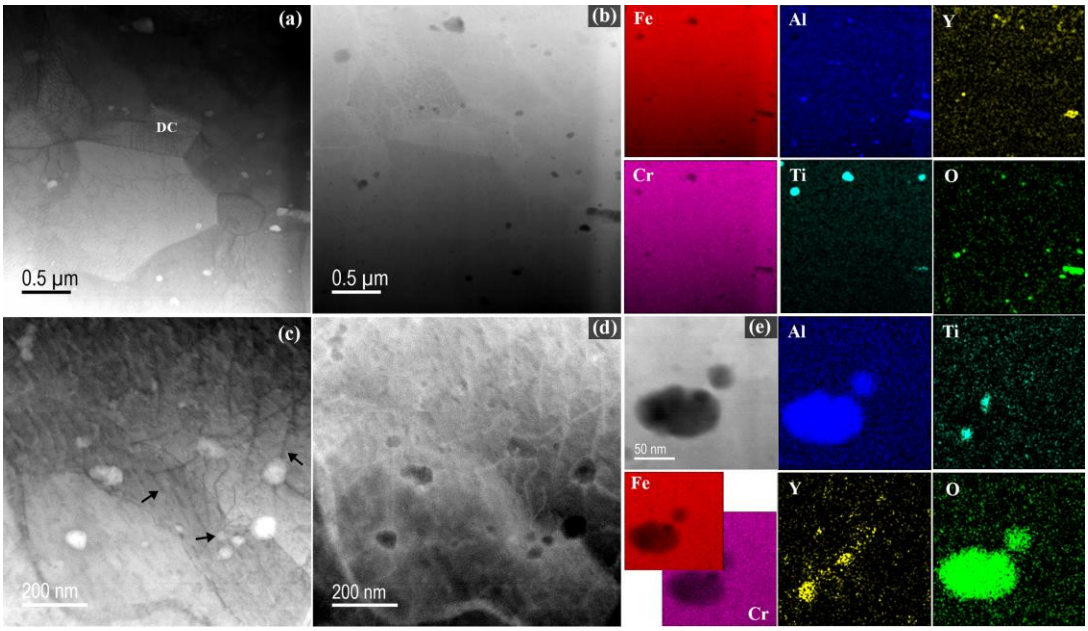

Figure 22. (a-b) BF and (c-d) corresponding HAADF STEM images of a sample cut along longitudinal direction of base metal PM2000 rod sample at two different resolutions. XEDS elemental maps to the top and bottom are for the area in (b), and a precipitate shown in (e).

Some of these dislocations and precipitates position along grain boundaries as well. As was observed in SEM/EDS analysis, majority of the precipitates are rich with Al. These Al-rich precipitates are also rich with oxygen, and Y is high in some parts of the precipitates. Ti-rich areas/precipitates are also present in the sample. These results show the presence of oxides, especially AlOx, YOy, and (Al, Y)Oz type oxides, and isolated elements (e.g., elemental Ti) in the as-received PM2000.

The same start section (Figure 23a) of the ShAPE extrudate used for other analyses was used to perform a focused ion beam (FIB) lift-out for TEM analysis. Figure 23b and c show SEM images of the area before and after FIB lift-out, which has been carried out at a location close to the intersection of the two different grain size distributions observed in the inner and outer diameters of the sample. The FIB lift-out for TEM analysis of the middle section of ShAPE extrudate was also performed at an area close to the center between inner and outer regions where small and large grains, respectively present. This sample area is highlighted in Figure 24.

TEM specimens prepared from the start and middle sections of the ShAPE-extruded PM2000 tube sample cut along longitudinal direction were imaged using STEM. As shown in the BF STEM image in Figure 25a, the bulk area of the TEM foil obtained from the start section consists of dark-contrast precipitates as was observed using SEM imaging. STEM images (Figure 25b-c) and the corresponding XEDS elemental maps of a selected precipitate show most of these precipitates are of (Al, Y)Oz type precipitates, while some are of AlOx and the rest are rich with Ti. The precipitates observed in the middle section of the extruded tube showed similar chemical composition (Figure 25d and the elemental maps). This observation is similar to that of the base metal, suggesting that the ShAPE did not affect the secondary precipitate composition significantly.

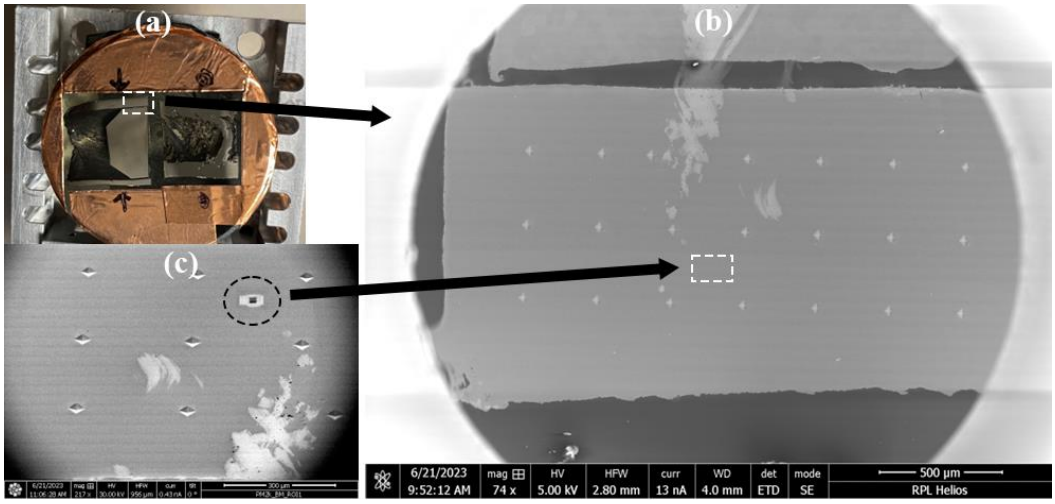

Figure 23. (a) SEM mount of the ShAPE-extruded sample highlighting the start section of interest, (b) SEM image of the area, and (c) SEM image of the area after FIB lift-out.

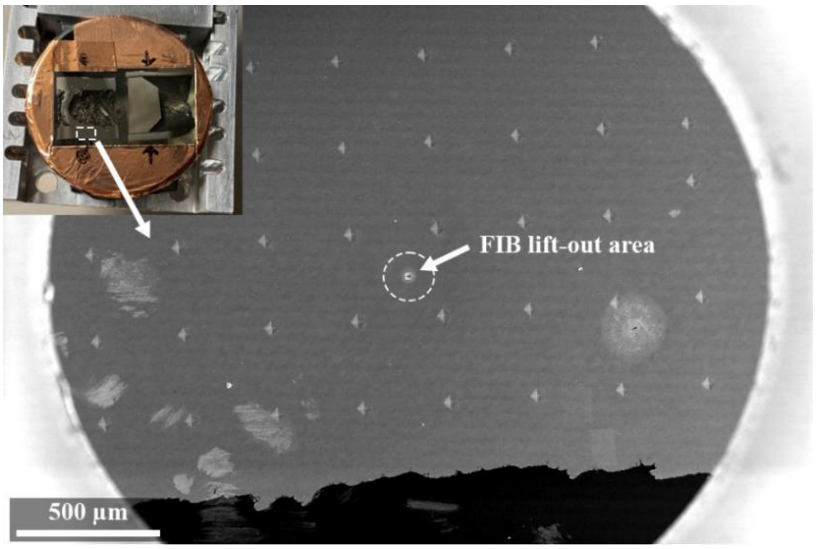

Figure 24. Inset shows the SEM mount highlighting the area with the area of interest (ROI2-2) of the middle section of ShAPE extrudate used for the SE SEM image with the FIB lift-out area highlighted.

FIB lift-outs were obtained at two different regions of the end section of the ShAPE extrudate cut along the longitudinal direction. These two regions were selected to represent regions 2 and 3 in Figure 26a. SEM images of the two regions together with the location of FIB lift-outs are also shown in Figure 26b and c, respectively. As shown in Figure 26b and c, regions 2 and 3 represent large (outer diameter region) and small (inner diameter region) grain areas, respectively. Also, region 3 was selected since it consisted of bulky square precipitates as observed using SEM (Figure 13f).

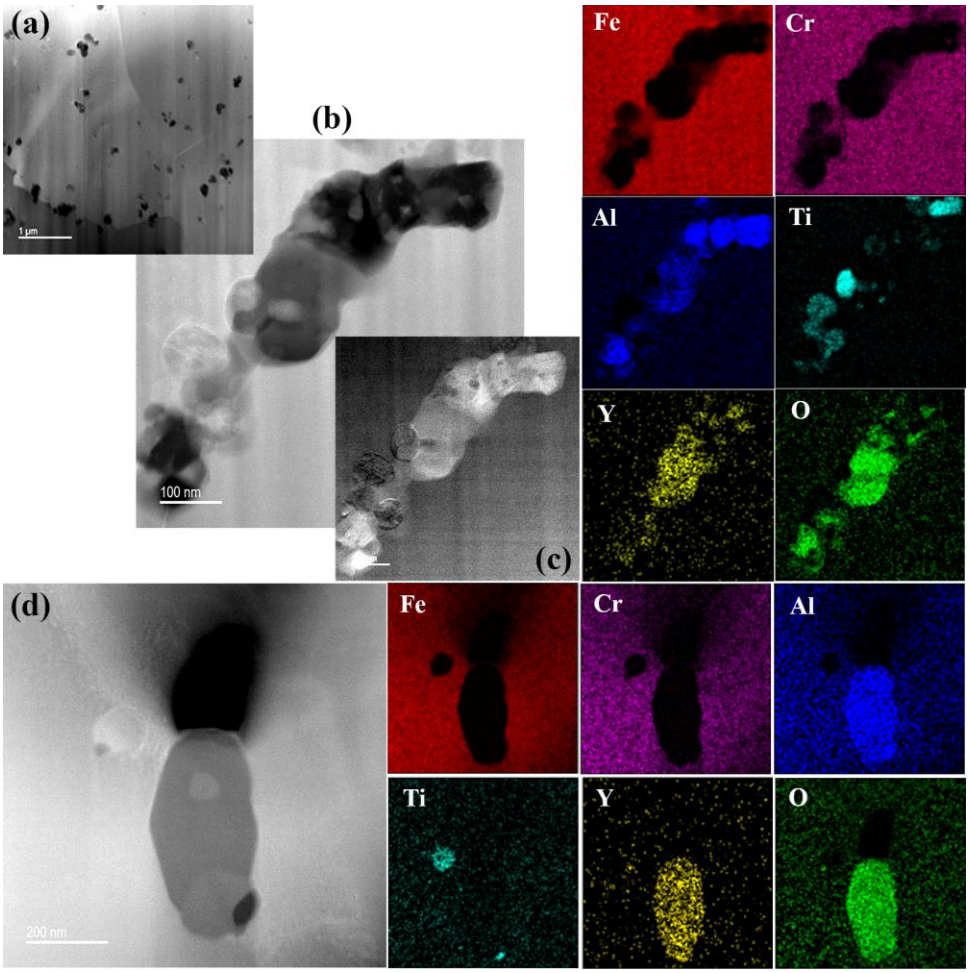

Figure 25. STEM images and XEDS maps of samples from a longitudinally cut sample of ShAPE-extruded PM2000 tube. (a) BF STEM image of a bulk area and (b) BF and (c) HAADF images of a precipitate from the start section of the tube sample, and (d) BF STEM image of a precipitate from the middle of the extruded tube sample.

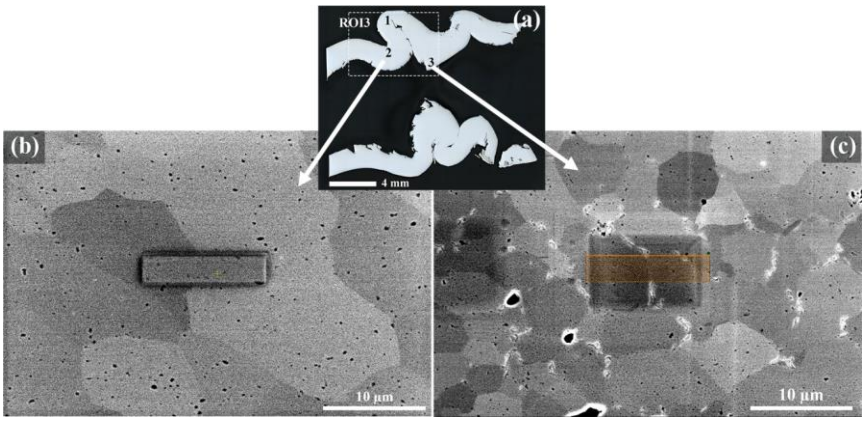

Figure 26. Optical micrograph showing regions of interest and BS SEM micrographs of regions 2 and 3 that used for the two FIB lift-out of longitudinally cut ShAPE extrudate at its end section.

As observed using SEM imaging, the end section of the extrudate (longitudinal direction) consists of precipitates as in the PM2000 base metal and the other sections of the ShAPE-extruded material. Furthermore, STEM imaging also confirmed the presence of considerably large amount of bulky square-type precipitates at the end section of the ShAPE extrudate of PM2000 (Figure 27a-b). The STEM image in Figure 27a is from the sample area of the end section of the ShAPE sample highlighted by number 2 in Figure 26a, while the image in Figure 27b is from the area highlighted as number 3 in Figure 26a. As shown in the elemental maps of Figure 27c, end section of the extrudate also consists of (Al, Y)Oz type precipitates with some Ti-rich precipitate areas. On the other hand, the bulky square-type precipitates are mostly rich with aluminum with no other second element present at a significant level in them. This observation suggests that the bulky square type precipitates are mostly segregated aluminum nano-precipitates formed as a result of the ShAPE.

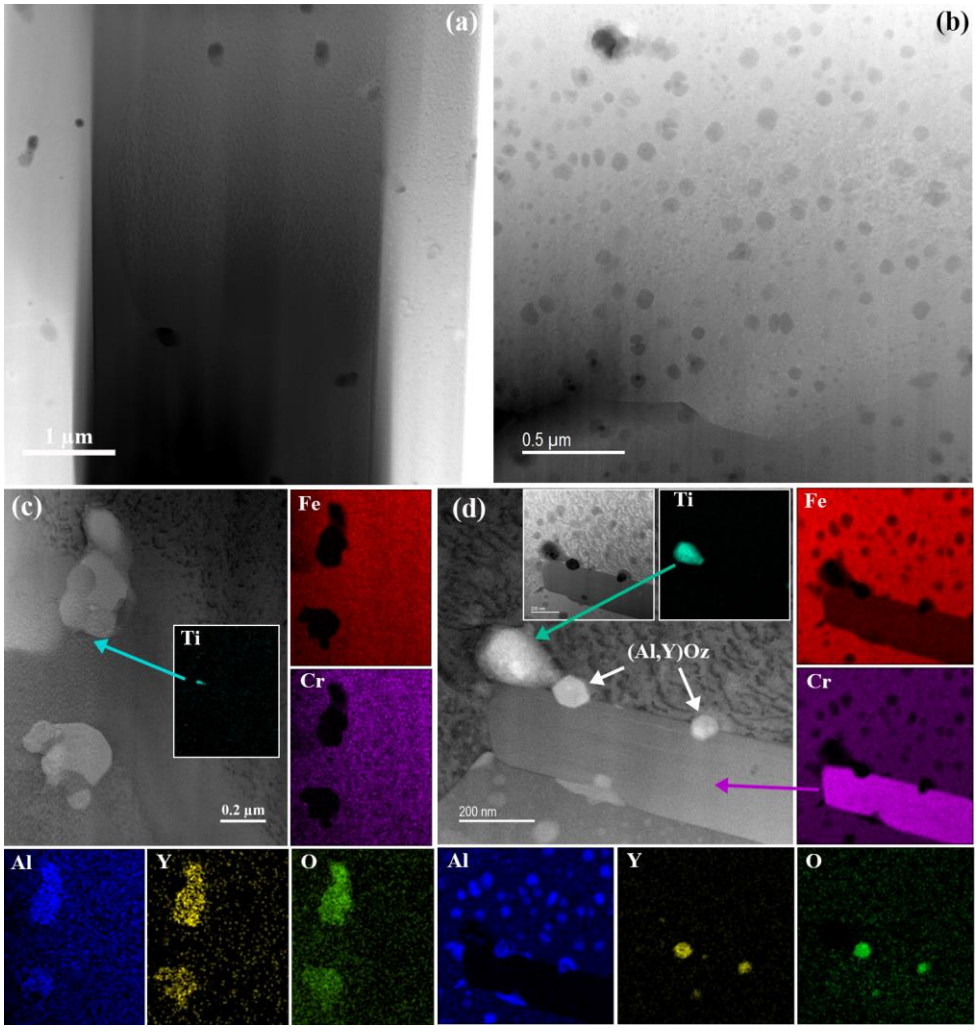

Figure 27. STEM images and XEDS maps of areas 2 and 3 in Figure 26a of the end section of a longitudinally cut sample of ShAPE-extruded PM2000 tube. BF STEM images of (a) less precipitate area and (b) cellular-type precipitate area. HAADF images of (c) less precipitate area and (d) bulky square type precipitate area. Inset of (d) is the corresponding BF image. The elemental maps are corresponding to the areas shown in (c) and (d).

2.6 Microhardness Data of As-Received and ShAPE-Extruded PM2000 Samples

The average Vickers microhardness value for PM2000 base metal rod (longitudinal) sample was 321 HV. The maximum, minimum and standard deviation (SD) values were 329, 311, and 4 HV, respectively. These results showed that the hardness was quite uniform (i.e., SD <4) across the sample (see Figure 28a). The average Vickers microhardness value for PM2000 base metal rod (transverse) sample was 329 HV and it is (Figure 28b) fairly similar to the longitudinal sample. The maximum, minimum and SD values in the transverse sample were 361, 313, and 11 HV, respectively, with a greater higher end value.

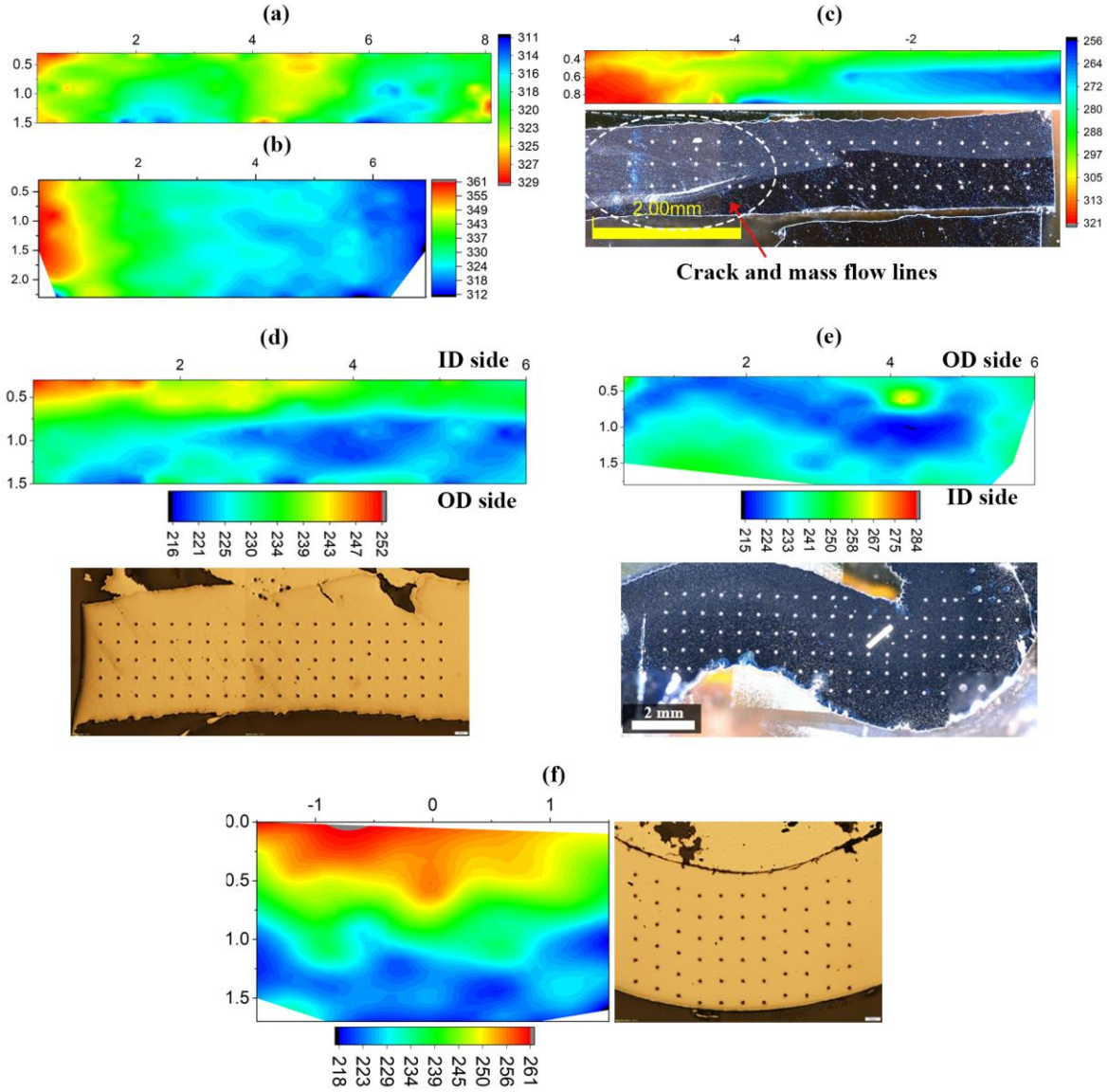

Figure 28. Vickers microhardness profile of PM2000 base metal rod. (a) Longitudinal sample; (b) transverse sample and ShAPE extruded samples in longitudinal direction: (c) start, (d) middle, (e) end, and (f) ShAPE extruded middle sample in transverse direction. Note that the color map shows the hardness in HV, while X and Y axes denote distance in millimeters.

As shown in Figure 6b, PM2000 ShAPE tube was cut into two halves and microhardness testing was performed on one of the tube walls (either top or bottom), in the longitudinal direction as shown in Figure 28c. The average Vickers microhardness value for ShAPE PM2000 sample (longitudinal) at the starting location was 290 HV. The maximum, minimum, and SD values were 321, 256, and 19 HV, respectively. Higher hardness values observed in the indented area near crack as expected (Figure 28c optical image). The grain size of PM2000 ShAPE longitudinal sample is slightly larger than that of the base metal (as shown in Figure 21a-b) and as a result its average hardness following the Hall-Petch relation (Hall, 1951, Petch 1953) is lower than the base metal. Figure 11a shows one of the cracks present in the sample. These cracks/openings are also consistent with extrusion-induced interfaces or mass flow lines corresponding to the material flow direction observed in that sample area. The outer part of the tube (Figure 11d) has a higher number of secondary metallic carbide precipitates than the inner part (Figure 11f), and it could have influenced this region to have higher hardness values (red and yellow regions). As mentioned earlier, these carbides have formed due to the ShAPE induced friction of the base metal and the tools utilized in the tube extrusion process.

The average Vickers microhardness value for ShAPE PM2000 sample (longitudinal) at the middle location was 230 HV. The maximum, minimum, and SD values were 252, 216, and 8 HV, respectively. The average and SD are much lower when compared to the starting location due to the absence of cracks and areas with reduced extrusion-induced interfaces or mass flow lines and reduced levels of carbides resulting from the ShAPE. The hardness is slightly higher near the ID when compared to the OD (Figure 28d) because the grain size is smaller at the ID region.

The average Vickers microhardness value for ShAPE PM2000 sample (longitudinal) at the end location (Figure 28e) was 231 HV. The maximum, minimum, and SD values were 264, 216, and 8 HV, respectively, and these values are quite like the middle location. The grain size of PM2000 ShAPE sample at middle and end locations was much larger than the starting location (HV 290) and base metal (HV 321), and this resulted in much lower hardness value (HV ~230), following the Hall-Petch relation.

The average Vickers microhardness value for ShAPE PM2000 sample along the transverse direction near the center of it (Figure 28f) was 237 HV, and it is like ShAPE (longitudinal) sample at both middle and end locations. The maximum, minimum, and SD values were 261, 218, and 13 HV, respectively. The hardness is slightly higher near the ID when compared to the OD since the grain size is smaller at the ID region. The grain size is much larger than the base metal in the transverse direction. Hence, its hardness (HV 237) is lower than the base metal (longitudinal HV 329) following the Hall-Petch relation.

2.7 Discussion

In both PM2000 base metal rod and ShAPE samples, Al- and Y-rich secondary precipitates, Al_2O_3 and/or $(Al, Y)_2O_3$ type oxides, and elemental Ti-rich particles could be identified from electron microscopy analysis. These data are also consistent with reported data on the Al- and Y-rich oxide precipitate composition of $YAlO_3$ in PM2000 alloy (Jung et al., 2017). As shown in Figure 29, the precipitate size increases in the order of base metal to start to the middle of the ShAPE sample, while end section of the ShAPE sample has smaller precipitate sizes than that of the middle section. The precipitate size in the middle and end sections of the ShAPE extruded tube samples are twice greater than the size of the base metal sample. The number density of precipitates shows an inverse proportionality to the change of their size, except for the bulky square-type Al-rich precipitates mostly identified at the end section of the ShAPE sample.

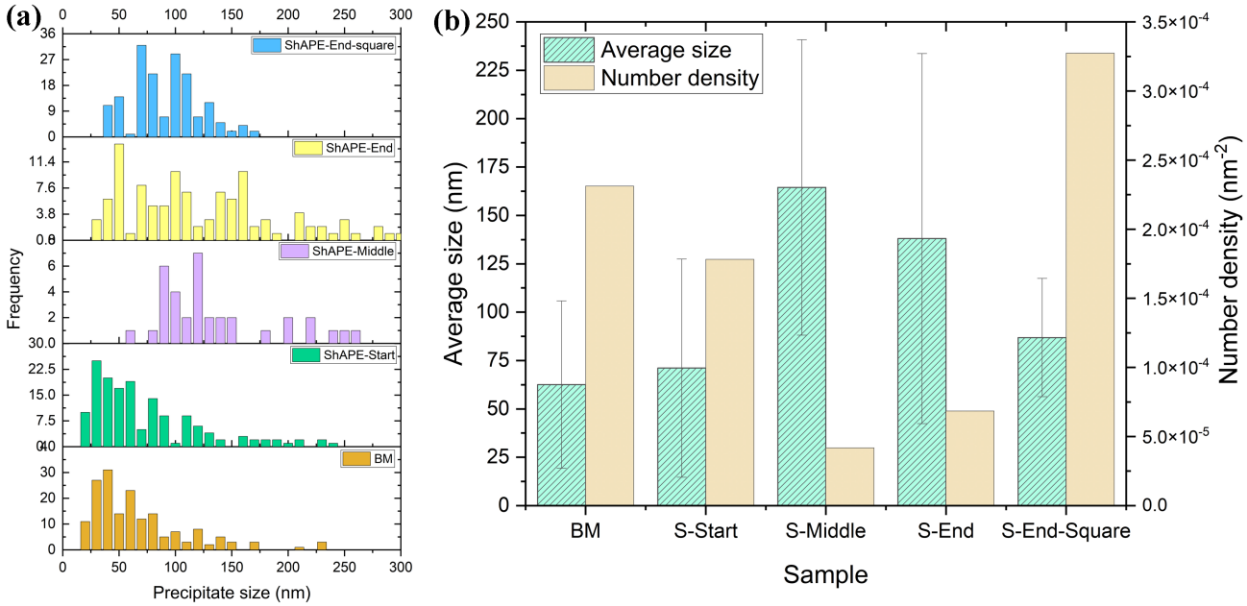

Figure 29. PM2000 base metal (rod) and ShAPE extruded tube samples. (a) Precipitate size distribution and (b) average precipitate size and density distributions. BM, S-Start, S-Middle, and S-End denote base metal, start, middle, and end sections of the ShAPE extrudate. S-End-Square denotes bulky square-type precipitates at the end section of the ShAPE tube.

The increase in the precipitate size and decrease in their density suggest ShAPE-induced growth of the secondary oxide particles but without significantly affecting the overall level of oxidation. This suggests that ShAPE might be used to refine ODS particles, but further experimentation is required to verify this observation. However, the moderate size and the highest density of bulky square-type precipitates observed at the end section of the extruded sample also suggest ShAPE-induced increase in the second phase precipitation.

A 0.04 to 0.07% smaller lattice parameter was also observed in the ShAPE samples compared to the base metal. While this small decrease in lattice parameters is usually not that significant, it can be attributed to the slight segregation of one or more of either Al, Y, and Ti from the α-ferrite since the atomic radii of Y and Ti are larger than Fe, Cr, and Al (Van der Walls radii of Fe, Cr, Al, Y, and Ti are 0.204, 0.206, 0.184, 0.232, and 0.211 nm, respectively) (Mantina et al., 2009). XRD analysis of bulk sample (an area of 10×10–15×15 mm^2) showed that the ShAPE reduced or fully removed the preferred orientation that was observed in the base metal PM2000.

A larger grain size distribution was observed in the ShAPE extruded samples than the base metal sample. Grain size was also greater in the outer diameter area than that of the inner diameter area of the ShAPE samples. In the longitudinally cut ShAPE samples, grain size increased with the progress from start section to the middle section of the tube extrusion. At the middle and end locations of the extruded tube, similar grain size distribution could be observed. These grain sizes are relevant to the ShAPE induced low to high temperature gradient in the inner to outer diameter region of the extrudate as low extrusion temperatures favor the formation of smaller grain sizes (Li et al., 2022b) The ShAPE induced extreme deformation might have introduced effective defects in the oxide phases and matrix destabilizing the oxide particles under certain conditions, and the enhanced diffusivity in the adjacent matrix could also allow coarsening and redistribution of an otherwise quite stable oxide phase.

Lower strain was observed in the ShAPE extruded tube samples than the base metal sample using EBSD analysis. The observation suggests intra-granular relaxation due to grain growth during extrusion. The overall reduction in the preferred orientation and strain further suggests greater microstructural homogeneity in the extrudate than that of the base metal that is typically observed in ShAPE extruded samples (Jata and Semiatin 2000, Overman et al., 2017).

The yield strength can be articulated as a combination of matrix strength and contributions from strengthening mechanisms. These mechanisms are based on limiting the mobility of dislocations moving through the lattice. For an ODS alloy used in this study, the strengthening mechanisms can be divided into solid solution strengthening, grain boundary strengthening, particle strengthening, and dislocation strengthening. The base matrix strength is the stress needed to move dislocations in the absence of other obstacles. For the PM2000 base metal and ShAPE-extruded material, these values are similar and close to the yield strength of the pure annealed iron. Strength of material can also be improved by the addition of solutes to the matrix by introducing strain field due to atomic radius misfit. The strain field acts as an obstacle when dislocation interacts with it. The composition of the present alloy is Fe–19.13%Cr–5.46%Al–0.48%Ti–0.39%Y (in wt.%). Solid solution strengthening contribution due to the addition of chromium and titanium has been investigated by other researchers (Lewis and Pickering, 1983). Al was reported to have little effect on the yield stress of steel (Pickering, 2007) due to its effect of combining with interstitial solutes of nitrogen and carbon. For the PM2000 base metal and ShAPE-extruded material because the Cr content is similar, there should not be any change due to solid solution strengthening effect.

The average Vickers microhardness value for PM2000 base metal rod longitudinal and transverse samples are quite similar, as shown in Table 2. The grain size of PM2000 ShAPE longitudinal sample is slightly larger than the base metal and as a result its average hardness following the Hall-Petch relation is lower than the base metal. Noh et al. also observed a similar decrease in hardness and tensile strength of an ODS ferritic steel after friction stir welding and attributed the decrease to grain coarsening (Noh et al., 2011). Darsell et al., 2018 also observed a similar reduction in hardness after ShAPE-extruding AZ91E flake due to grain coarsening. Grain boundaries can act as barriers to dislocation motion. The dislocation pileups against grain boundaries can create back stress to the moving dislocation and thus provide strengthening. Larger grain structure was observed in PM2000 ShAPE material when compared to the base material, which led to reduced grain boundary strengthening contribution.

Table 2. Microhardness test results of various PM2000 samples.

PM2000 Sample	Average HV	Max HV	Min HV	Std. Dev. HV
Base metal rod (longitudinal)	321	329	311	3.83
Base metal rod (transverse)	329	361	313	11.29
ShAPE (starting location)	290	321	256	19.37
ShAPE (middle location)	230	252	216	8.34
ShAPE (end location)	232	284	216	9.30
ShAPE (transverse – middle)	237	261	218	12.55

The grain size of PM2000 ShAPE sample (longitudinal) at middle and end locations was much larger than the starting location that has a hardness of HV 290 and base metal with a hardness of HV 321, and this resulted in much lower hardness value of HV ~230, following the Hall-Petch relation. The average Vickers microhardness values for ShAPE PM2000 samples (longitudinal - middle and end locations) were quite similar to ShAPE PM2000 transverse sample, since the large grain size distributions, especially in the outer diameter area, in these samples were very

similar and also due to the reduction in the anisotropy (longitudinal vs. transverse). Other researchers also observed similar reduced anisotropy and hardness values before and after ShAPE-extruding Mg alloys (Whalen et al., 2019).

Some of the samples showed cracks/openings and these were consistent with extrusion-induced interfaces or mass flow lines corresponding to the material flow direction observed in that sample area. The outer part of the tube has a higher number of secondary metallic carbide precipitates than the inner part, and it could have influenced this region to have higher hardness values. As mentioned earlier, these carbides were formed due to the ShAPE induced friction of the base metal and the tools used in the tube extrusion process. Generally, the hardness is slightly higher near the ID when compared to the OD since the grain size is smaller at this region. These observations suggest a continuous grain growth from the base metal to ShAPE extruded tube due to the ShAPE-induced grain growth or recrystallization with lowest grain growth effect on the inner part of the extrudate as is observed in other reported studies carried out using ShAPE (Overman et al., 2017).

The presence of nano-sized dispersoids in an ODS alloy can impede dislocation motion and dislocations must overcome it by looping around the non-shearable particles. As a result, the yield strength of the material is increased. The particle strengthening can be expressed by the Orowan equation (Brown and Ham, 1971). At the starting location, the average precipitate size and number density were found to be slightly larger and lower when compared to the base material. However, the average precipitate size and number density were found to be much larger and lower at middle and end locations, thereby resulting in lower strength at these locations (middle and end) due to reduced particle strengthening contribution.

3.0 ShAPE Manufactured 14YWT ODS Steel

Experimentation with 14YWT powder Batch 1 (batch unique identifier 14YWT-V540-01-40H 3) was undertaken as this specific powder has been used for research previously conducted by Dr. Stuart Maloy, Dr. David Hoelzer, and Prof. G. Robert Odette and the production of the 14YWT powder was funded by the DOE Global Nuclear Energy Partnership program in 2008 subcontract-70553-001-09. The benefit of using this powder is that the result of the properties obtained from the advanced manufacturing techniques used in this study, can be benchmarked. This benchmark comparison will be performed in the final phase of this project. Although ShAPE bar manufacturing of GARS powder occurred, this will be the first direct manufacturing of *tubing* using 14YWT ODS steel powder.

This section report only preliminary development and characterization results of three tube ShAPE experiments consistent to proof feasibility and to the level of funding available for this project.

3.1 Characteristics of Mechanically Alloyed 14YWT ODS Steel Powder Batch 1

The chemical composition of the 14YWT powder was provided with the material and is captured in Table 3 as analysis A1, performed in November 2020. A sample of the material was sent to an outside vendor for chemical composition analysis via inductively coupled plasma mass spectrometry (ICP-MS) in January 2023. These data also are given as analysis A2. The two chemical compositions are comparable with the oxygen concentration remaining constant, indicating the alloy is resistant to oxidation at room temperature. Slight differences in concentration were observed for other elements analyzed, which could be attributed to a single data point and associated uncertainty of the method.

Table 3. Chemical composition of 14YWT.

ICP-MS	O	N	C	H	Fe	Cr	Y	W	Ti	Mn	Ni	Cu	Al	Si	Zr
A1-Wt%	0.097	nm	0.008	nm	nm	13.6	0.25	3.12	0.41	0.020	0.041	0.037	0.012	nm	nm
A2-wt%	0.119	0.007	0.011	0.002	81.59	14.4	0.21	3.12	0.40	0.019	0.016	0.004	0.022	0.062	<0.002

Powder size distribution was determined by two methods: 1) laser diffraction and 2) SEM imaging (Table 4). For particle size analysis using laser diffraction, 0.1 g of 14YWT was added to 30 mL of deionized water and three to five drops of TWEEN® 20 dispersant. The mix was sonicated 20 times to 9 watts by Microson ultrasonic cell disruptor to suspend the alloy powder in the deionized water/TWEEN 20 mixture. A Microtrac Sync M5000 was used to measure dynamic particle size and shape. The particle size distribution (PSD) plot is shown in Figure 30

Table 4. PSD of as-received 14YWT.

PSD by Vol%	Size, µm Laser Diffraction	Size, µm SEM ImageJ
d10	51.6	126.8
d50	102.5	190.3
d90	248	299

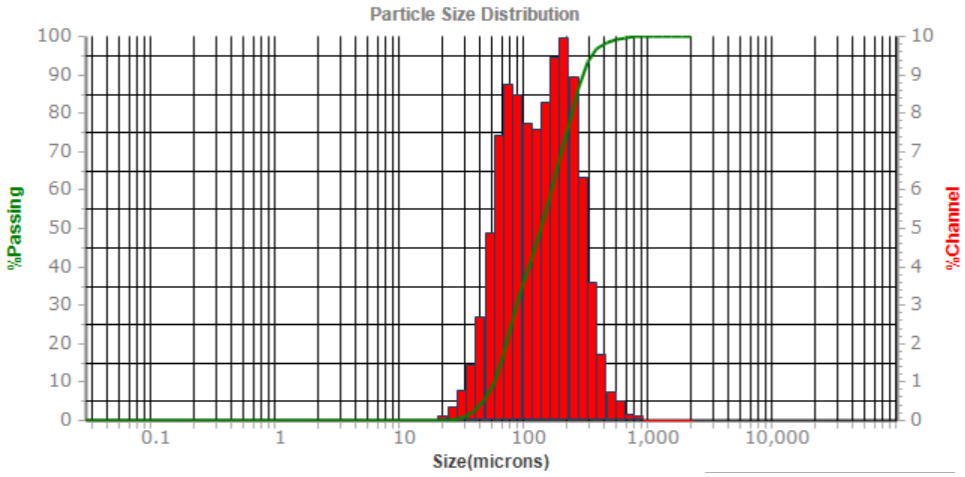

Figure 30. PSD of as-received 14YWT powder.

A bimodal distribution of powder size is noted, with the first peak being slightly below 100 µm and the second peak close to 200 µm. The as-received powder feedstock has a good mix of relatively fine and coarse particles. The as-received 14YWT powder also was analyzed using SEM to gain insight of the particle morphology. The PSD analysis of the as-received 14YWT material indicated that the powder is coarse, and the packing density and other process parameter optimization may be challenging for densification through solid-state sintering, which is the final mechanism through which FFF-built parts attain high density.

SEM imaging, shown in Figure 31, was performed using JEOL JSM-7600F secondary electrons with an accelerating voltage of 10 kV. The powder is highly magnetic and requires careful handling within the SEM. To help combat the highly magnetic nature of the particles, a larger working distance of 15 mm was chosen to avoid damage to the pole piece on the SEM.

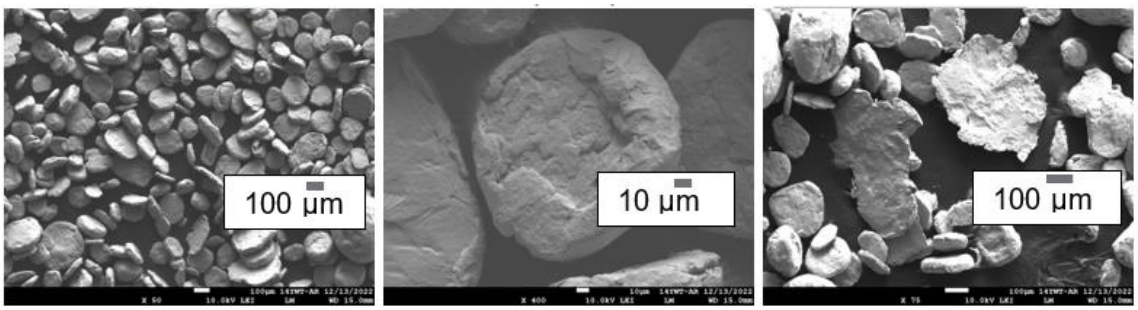

Figure 31. SEM images of as-received 14YWT powder.

The as-received 14YWT powder has a flat, disc-like morphology typical of the mechanical milling process. There are some very large particles with diameters over 300 µm. SEM imaging confirms that the particle size is larger and does not have the high specific surface area (area/volume) needed for densification through sintering. ImageJ was used to perform image analysis to determine the PSD, select percentiles are presented in Table 4.

Based on the initial characterization of as-received 14YWT powder, the alloy was confirmed to have the reactive elements (Y and Ti) and dissolved oxygen needed for the formation of fine and thermally stable oxide particles (Y-Ti-O based) after heat treatment to provide strength at high temperature.

3.2 Densification of 14YWT ODS Powder using SPS for SHAPE Billets

As the 14YWT powder was mechanically alloyed and flakey, and initial challenges were experienced for the sintering process as part of the earlier FFF work, we decided to use a densification process to produce the input billets (i.e., the feedstock) for the ShAPE equipment. Various densification processes could be followed as shown in Figure 2, and SPS was chosen for our first ODS SHAPE experimentation.

3.2.1 SPS Process Parameters and Preliminary Properties

The SPS sinter temperatures were kept lower than normal for full densification as we wanted to keep temperatures as low as possible for potential grain growth during densification as the full powder size-microstructure-manufacture-property relationships are not established yet for these materials. Table 5 describes the SPS Densification parameters and result of 14YWT ODS Powder for ShAPE Billets while Figure 32 show the associated SPS processing cycles for the ShAPE billet forming from 14YWT powder.

Table 5. SPS densification of 14YWT ODS powder for ShAPE billets.

Sample #	Target pressure	Target temperature	Process parameters	Density	Vickers microhardness (300 gf; 15 s dwell)
1	35 MPa (pressure loaded before heating)	1050°C (0 - 900° @ 50°C/min. 900-1050°C @ 25°C/min) Dwell @ 1050C (15 minutes)	15 min dwell Argon environment ~65g of powder 1.25'' diameter die	(7.384 g/cm^3) 95.48%	
2 **(Impact of increased pressure)**	35MPa before heating Increase to 50MPa starting at 900C x 5MPa/min	1050°C (0 - 900° @ 50°C/min. 900-1050°C @ 25°C/min) Dwell @1050C (15 minutes)	15 min dwell Argon environment ~65g of powder 1.25'' diameter die	(7.509 g/cm^3) 97.09%	Max: 402.08 HV Min: 134.84 HV SD: 86.80 HV Total number of indents: 56.
3 **(Impact of increased dwell time at 1050°C)**	35MPa before heating	1050°C (0 - 900° @ 50°C/min. 900-1050°C @ 25°C/min) Dwell @1050C (30 minutes)	30 min dwell Argon environment ~65g of powder 1.25'' diameter die	(7.388 g/cm^3) 95.53%	
4 **(Impact of running at lower temp and lower dwell time to reduce ODS particle growth)**	35MPa before heating Increase to 50MPa starting at 850C x 5MPa/min	950°C (0 - 900° @ 50°C/min. 900-950°C @ 25°C/min) 950°C: We want to be below 1,000°C to limit the ODS particle growth. Hold temp at 850°C during pressure application. Once pressure is done go up to 950°C.	60 min dwell Argon environment ~65g of powder 1.25'' diameter die	(7.291 g/cm^3) 94.28%	Max: 504.57 HV Min: 155.64 HV SD: 112.54 HV Total number of indents: 58

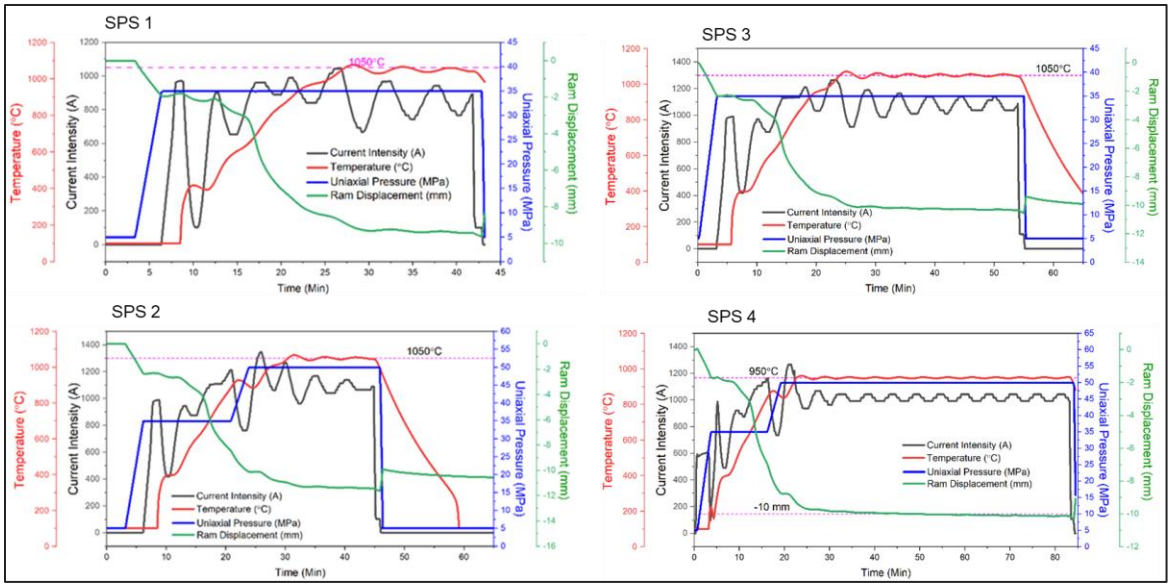

Figure 32. SPS processing cycles for the ShAPE billet forming from 14YWT powder.

3.2.2 Microstructural Examination of As-Received SPS Samples

As shown in Figure 33a-c, 14YWT SPS sample 2 has a bimodal grain microstructure. It also consists of some pore spaces as highlighted in Figure 33b and at least two different precipitates: bright-contrast and dark-contrast (Figure 33c). Some areas also contain long microcracks as depicted in Figure 33d.

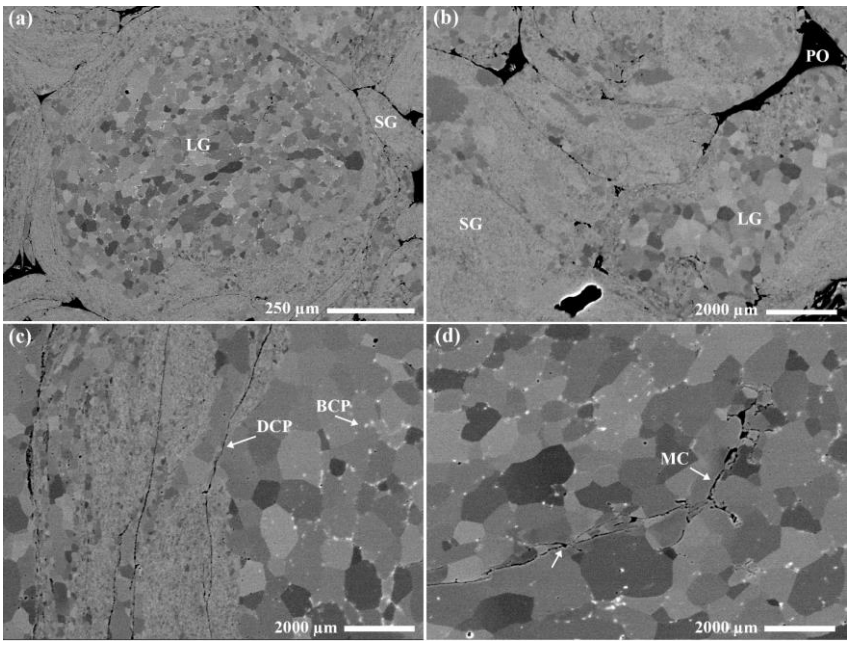

Figure 33. BSE SEM micrographs of 14YWT sample mount 2. (a–b) Bimodal grain distribution in two different resolutions, (c) Bright contrast precipitates, and (d) microcracks of the sample. LG, SG, PO, BCP, DCP, and MC denote large grains, small grains, bright-contrast precipitates, dark-contrast precipitates, and micro cracks, respectively.

The bright-contrast precipitates were mostly observed along grain boundaries of the large grains (Figure 34a). These precipitates are rich with W, Y, and Ti as shown in the elemental maps corresponding to the sample area depicted in Figure 34a. While dark-contrast precipitates on these grains mostly contain Y, dark-contrast precipitates accumulated along grain boundaries (and grain boundary cracks) that separate large grains from small grains contain Ti and oxygen as shown in the elemental maps corresponding to the area depicted in Figure 34b.

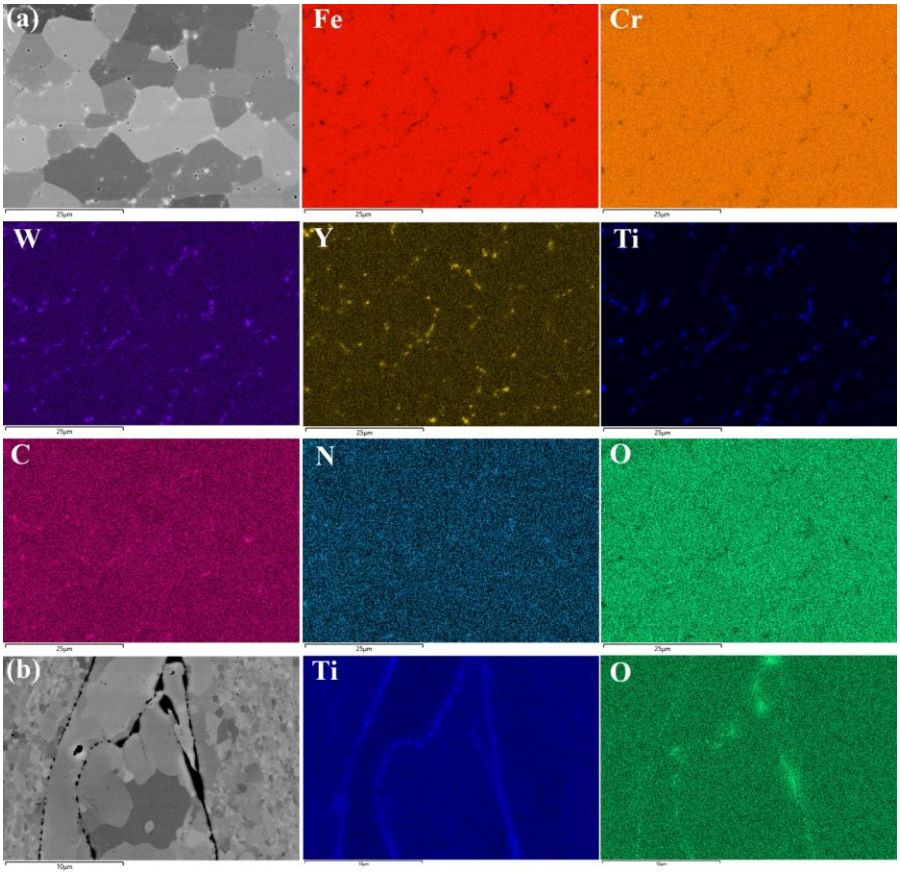

Figure 34. Elemental maps of two different areas of 14YWT sample.

EBSD data also confirmed the presence of bimodal grain distribution of the 14YWT sample (Figure 35). The average grain size of small grains is 0.8 ±0.9 µm and large grains are 6.3 ±3.9 µm. The large grains distribute in a grain size range of ~1–22 µm, while the size of small grains span ~0.2–6 µm range.

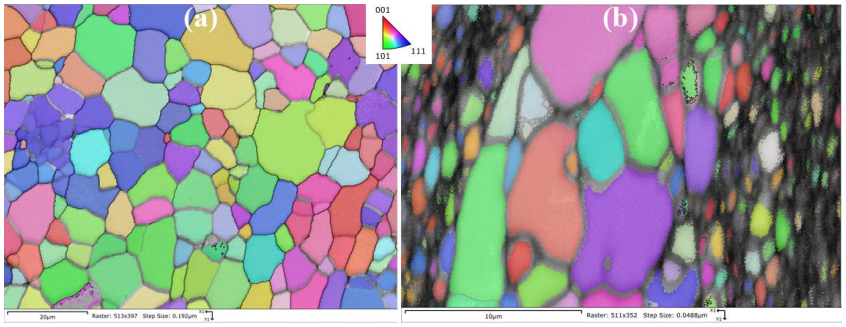

Figure 35. Orientation maps of 14YWT sample at two different resolution and areas.

3.3 ShAPE Experimentation of 14YW4T ODS SPS Billets

Figure 36a shows friction stir welder that was used to extrude ODS ShAPE tubes. The ShAPE working principle is shown in Figure 36b wherein a rotating die with an extrusion orifice interacting with the feedstock thereby producing a tube between the mandrel and inner diameter of the die.

ShAPE experiments with SPS Billets 2, 4, and 3 were conducted as experiments 2, 3 and 4 respectively. The ShAPE processing characteristics of 14YWT SPS billets were significantly different from wrought PM2000 as shown in Figure 37. Ram velocity was similar between the first and second runs while spindle speed was reduced in the second run as compared to the first run. However, the second run (SPS feedstock Billet 2) had similar die temperature as the first run (solid PM2000 feedstock) Die temperature near and end of 5 mm/min ram velocity was about 1,128 and 1,188°C, respectively. Ram force had different trend in the second run as compared to the first run. The second run had a peak force of 120 kN as compared to about 60kN near the end of first run. After the peak, the force slowly reduced and reached about 12 kN. This was not the case with the first run and could be due to porosity in the sample.

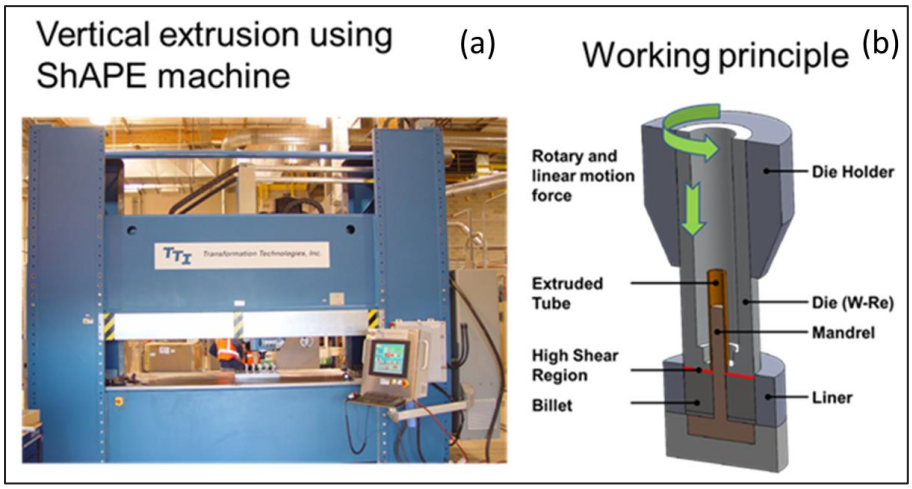

Figure 36. (a) Friction stir welder used to fabricate ODS ShAPE tube and (b) ShAPE working principle.

The results of the ShAPE experiments are shown in Figure 38. Comparing the second and third ShAPE experiments: Ram velocity was increased by approximately five times during the third experiment as compared second experiment. The main reason to do that was to process at increased force to potentially increase consolidation. Both force and torque were higher during the third experiment as compared with the second run. Furthermore, oscillations in force and torque were noted, like the second run. Die temperature increased throughout the third run signifying that steady state was not reached; hence, further refinement in processing conditions to obtain a tube from SPS billets is needed. The die temperature near the start and end of 25 mm/min ram velocity was about 517°C and 1,176°C, respectively. For the fourth experiment, only ram velocity was changed to 15 mm/min. A maximum die temperature of 1,270°C was noted and due to flash generation, the thermocouple was damaged around 5.5 mm plunge depth. Characterization of these extrudates could not yet be performed to determine if there are any differences in the ODS particle size or distributions after exposed to the combined effect of SPS and ShAPE extrusion. Specifically, the third experiment using SPS billet 4, did not reach steady state; therefore, the microstructure resulting would not provide conclusive evidence yet.

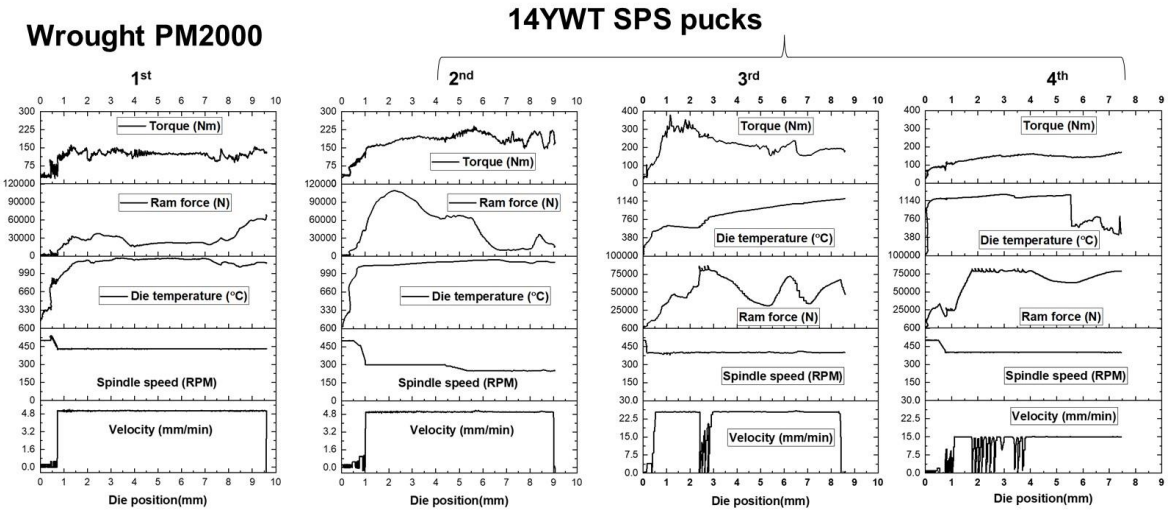

Figure 37. Summary of ShAPE process input and output for the four ShAPE experiments completed for ODS steels.

Figure 38. Summary of preliminary results.

4.0 Conclusions on Feasibility Study on ShAPE Tube Forming of ODS Steel

This study provides the first-of-a-kind results of direct tube formation though ShAPE for ODS steel material. Previously only bar shapes have been successfully made.

This study provides preliminary information on development of ShAPE tube forming of ODS directly from stock material, and not via an interim step of bar and pilgering as one of the current manufacturing methodologies. These experiments also aimed to determine sensitivity toward mechanically alloyed ODS powder, as previously, successful bar feedstock manufacturing was performed with highly specialized spherodized powder. The full solid-state manufacturing feasibility study will be completed and reported in a final feasibility evaluation during 2025. The study investigation used two types of ODS steel feedstock billets namely 1) uncrystallized ODS PM2000 alloy (Fe20Cr5Al) purchased from Plansee USA LLC and 2) SPS billets fabricated for the AMMT program from 14YWT powder (batch unique identifier 14YWT-V540-01-40H 3) funded by the DOE Global Nuclear Energy Partnership program in 2008 subcontract-70553-001-09. The benefit of using this powder is that the result of the properties obtained from the AM techniques used in this study, can be benchmarked. This benchmark comparison will be performed in the final phase of this project.

The first ShAPE experiment completed on the PM2000 billet yielded an approximately 4-inch length of tube and shows in principle the feasibility of the direct tube fabrication in a single step while recognized that full steady-state conditions were not reached during the first experiment, and that process optimization should still be performed on this specific material conditions. A detailed microstructural analysis, although showing variations between the start, middle and end sections, shows that conditions towards the end were more consistent and can be built upon during next studies. However, the results, both in understanding the process parameters and behavior in relationship with the microstructural variations, can provide valid input to the modeling efforts, although not funded under the AMMT program, can minimize future experiments. Specific observations from the PM2000 extrudate tube are described below:

- Al- and Y-rich secondary precipitates, Al_2O_3 and/or $(Al, Y)_2O_3$ type oxides, and elemental Ti-rich particles could be identified from electron microscopy analysis.
- The precipitate size increases during SHAPE processing to approximately double the base material size, although the precipitate sizes of the end section are smaller than the mid-section.
- The number density of precipitates shows an inverse proportionality to the change of their size, except for the bulky square-type Al-rich precipitates mostly identified at the end section of the ShAPE sample. The increase in the precipitate size and decrease in density suggest ShAPE-induced growth of the secondary oxide particles but without significantly affecting the overall level of oxidation. This suggests that ShAPE might be used to refine ODS particles, but further experimentation is required to verify this observation. However, the moderate size and the highest density of bulky square-type precipitates observed at the end section of the extruded sample also suggest ShAPE-induced increase in the second phase precipitation.

Compared to the wrought PM2000, all the experiments with SPS Billets as feedstock had resulted in fractured tubes. This could be due to the porosity in the SPS consolidated feedstocks. An early conclusion is therefore that the stock material for the current feasibility shows that less than 97% dense feedstock is not sufficient for ODS materials for direct tube forming. However, another aspect that needs to be considered that has not been established, is how the bimodal grain sizes influence the consistency and flow during the extrusion process. Characterization of these extrudates could not yet be performed to determine if there are any differences in the ODS particle size or distributions after exposed to the combined effect of SPS and ShAPE extrusion. Specifically, the third experiment using SPS billet 4 did not reach steady state; therefore, the microstructure resulting would not provide conclusive evidence yet.

Finally, the four ShAPE experiments conducted show feasibility regarding fabricability for ODS tube forming was shown, although optimization for microstructure repeatability would need to receive attention with follow-up work; therefore, the combination of results reported here, together with the separate studies by other PNNL researchers on bar fabrication of ODS, provide the justification for early Technical Readiness Level feasibility.

5.0 Reports, Publications and Presentations

One peer-reviewed journal publication has been submitted for review to date from this work:

- Silva, C.M., M. Komarasamy, J. D. Escobar, S. Tripathi, R. Prabhakaran, Q. R. S. Miller, T. A. Ajantiwalay, M. J. Olszta, I. J. van Rooyen. (2024b) Submitted to Material Science & Engineering A, September 2024

6.0 References

ASTM E384, 2022. "Standard Test Method for Micro-indentation Hardness of Materials." ASTM International, West Conshohocken, PA.

Azushima, A., Kopp, R., Korhonen, A., et al., 2008. “Severe plastic deformation (SPD) processes for metals.” CIRP Annals 57(2) 716-735.

Briggs, S. A., P. D. Edmondson, K. C. Littrell, Y. Yamamoto, R. H. Howard, C. R. Daily, K. A. Terrani, K. Sridharan, K. G. Field. 2017. “A combined APT and SANS investigation of α′ phase precipitation in neutron-irradiated model FeCrAl alloys.” Acta Mater. 129: 217e228.

Brown, L. M. and Ham, R. K. 1971. *Dislocation-particle interactions.* R. B. Kelly. 1971. *Strengthening Methods in Crystals*. Nicholson (Eds.). Elsevier. Amsterdam: 9–135.

Burns, Carolyne A., Saumyadeep Jana, Amrita Lall, Zachary C Kennedy, Michelle D Fenn, Joshua A Silverstein, Lorraine M Seymour, Isabella J Van Rooyen. 2023. “Preliminary Characterization and Evaluation on FFF Manufactured 316H and ODS Steels.” PNNL-34985, September 2023

Capdevila, C., M. K. Miller, I. Toda, J. Chao, 2010. “Influence of the α–α′ phase separation on the tensile properties of Fe-base ODS PM2000 alloy.” Mater. Sci. Eng. 527 (2010) 7931e7938.

Darsell, J. T., N. R. Overman, V. V. Joshi, S. A. Whalen, and S. N. Mathaudhu. 2018. “Shear Assisted Processing and Extrusion (ShAPE™) of AZ91E flake: a study of tooling features and processing effects.” *J. Mater. Eng. Perf.* 27: 4150–4161.

Dryepondt, A. Rouaix-Vande Put, B.A. Pint. 2013. “Effect of H_2O and CO_2 on the oxidation behavior and durability at high temperature of ODS-FeCrAl.” Oxid. Met. 79 (2013) 627–638.

Dryepondt et. al., 2018. “Development of low-Cr ODS FeCrAl alloys for accident-tolerant fuel cladding.” Journal of Nuclear Materials 501 (2018) 59-71

Field, K. G., X. Hu, K. C. Littrell, Y. Yamamoto, L. L. Snead. 2015. “Radiation tolerance of neutron-irradiated model Fe-Cr-Al alloys.” J. Nucl. Mater. 465 (2015) 746e755.

Hall. E. O. 1951. “The deformation and ageing of mild steel: III discussion of results.” *Proc. Phys. Soc., Sect. B* 64 (9): 747–755.

Jata, K., and S. Semiatin. 2000. “Continuous dynamic recrystallization during friction stir welding of high strength aluminum alloys.” 2000. *Air Force Research Lab Wright-Patterson AFB OH Materials and Manufacturing*.

Jung, H. J., D. J. Edwards, R. J. Kurtz, T. Yamamoto, Y. Wu, and G. R. Odette. 2017. “Structural and chemical evolution in neutron irradiated and helium-injected ferritic ODS PM2000 alloy.” *J. Nucl. Mater.* 484: 68–80.

Komarasamy M., Lei Li, B. Taysom, B. Taysom, A. Soulami, G. Grant, D.Herling and S. Whalen. 2022. “Co-Extrusion of Dissimilar Aluminum Alloys via Shear-Assisted Processing and Extrusion.” Light Metals 2022, 308-313

Lewis, D. B., and Pickering, F. B. 1983. “Influence of aluminium and thermomechanical treatment on formability and mechanical properties of type 430 stainless steel.” *Met. Technol.* 10: 264–273.

Li, M., D. Andersson, R. Dehoff, A. Jokisaari, I. van Rooyen, D. Cairns-Gallimore,2022a. “Advanced Materials and Manufacturing Technologies (AMMT) 2022 Roadmap.” ANL-23-12, September 2022.

Li, L., Reza-E-Rabby, M., Overman, N., Wang, T., Whalen, S., Grant, G., Mathaudhu, S., and Soulami. A. 2022b. “Analysis of contact conditions and microstructure evolution in shear assisted processing and extrusion using smoothed particle hydrodynamics method.” Mater. Des. 221: 111010.

Mantina, M., A. C. Chamberlin, R. Valero, C. J. Cramer, and D. G. Truhlar. 2009. “Consistent van der Waals radii for the whole main group.” J. Phys. Chem. A 113: 5806–5812.

Marechal, B. Lesage, A. M. Huntz, R. Molins. 2003. “Oxidation behavior of ODS Fe-Cr-Al alloys: Aluminum depletion and lifetime.” Oxid. Met. 60 (2003) 1–28.

Noh, S., R. Kasada, A. Kimura, S. H. C. Park, and S. Hirano. 2011. “Microstructure and mechanical properties of friction stir processed ODS ferritic steels.” J. Nucl. Mater. 417: 245–248.

Overman, N. R., S. A. Whalen, M. E. Bowden, M. J. Olszta, K. Kruska, T. Clarkc, E. L. Stevens, J. T. Darsell, V. V. Joshi, X. Jiang, K. F. Mattlin, and S. N. Mathaudhu. 2017. “Homogenization and texture development in rapidly solidified AZ91E consolidated by Shear Assisted Processing and Extrusion (ShAPE).” Mater. Sci. Eng. A. 701: 56–68.

Petch, N. J. 1953. “The cleavage strength of polycrystals.” *J. Iron Steel Inst.*, 174 (1): 25–28.

Pickering, F.B., 1977. *High strength low alloy steels: a decade of progress. Korchynsky (Ed.), Microalloying* ’75, Union Carbride Corp, New York: 9–31.

Silva, C.M., M. Komarasamy, J. D. Escobar, S. Tripathi, R. Prabhakaran, Q. R. S. Miller, T. A. Ajantiwalay, M. J. Olszta, I. J. van Rooyen. 2024a. A discussion on microstructural and mechanical characteristics of ShAPE extruded PM2000 FeCrAl tubes, TMS2024, March 3–7, 2024, Hyatt Regency Orlando, Orlando, Florida, USA

Silva, C.M., M. Komarasamy, J. D. Escobar, S. Tripathi, R. Prabhakaran, Q. R. S. Miller, T. A. Ajantiwalay, M. J. Olszta, I. J. van Rooyen. 2024b. "Shear assisted processing and extrusion (ShAPE) of ferritic ODS PM2000." PNNL-SA-204107. Submitted to Material Science & Engineering A, September 2024

Tuncer, N. and A. Bose. “Solid State Manufacturing: A Review.” 2020. JOM, Vol. 72, No. 9, 2020.

Whalen, S., N. Overman, V. Joshi, T. Varga, D. Graff, and C. Lavender. 2019. “Magnesium alloy ZK60 tubing made by Shear Assisted Processing and Extrusion (ShAPE).” *Mater. Sci. Eng. A.* 755: 278–288.

Whalen, S., B. Taysom, N. Overman, Md. Reza-E-Rabby, Y. Qiao, T. Richter, T. Skszek, M. DiCiano. 2023. “Porthole die extrusion of aluminum 6063 industrial scrap by shear assisted processing and extrusion.” Manufacturing Letters, Volume 36, July 2023, Pages 52-56

Zhang, D., J.T. Darsell, J. Wang, X. Ma, G.J. Grant, I.E. Anderson, J.R. Rieken, D.J. Edwards, W. Setyawan, T.J. Horn, G.R. Odette. 2022. “No ball milling needed: Alternative ODS steel manufacturing with gas atomization reaction synthesis (GARS) and friction-based processing.” Journal of Nuclear Materials, Volume 566, 1 August 2022, 153768 https://www.sciencedirect.com/science/article/pii/S0022311522002550?via%3Dihub

Appendix A – Supporting XRD data

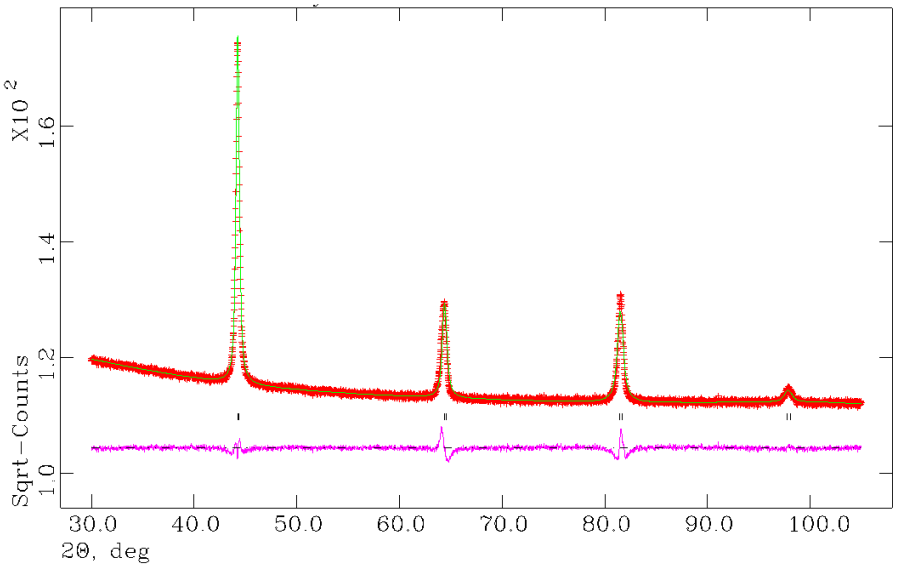

Figure A.1. XRD pattern of the base metal PM2000 along its longitudinal direction. Red, green, and pink color are the experimental, calculated, and difference patterns, respectively. The black color tick marks indicate the peak positions of α-ferrite phase.

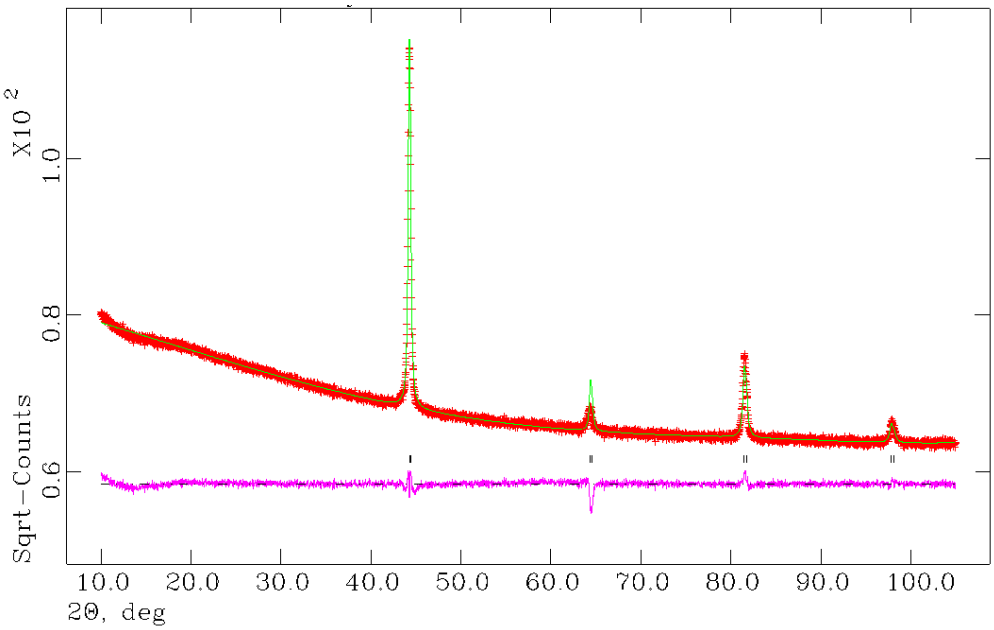

Figure A.2. XRD pattern of the longitudinally cut ShAPE extrudate together with its Rietveld fit. Red, green, and pink color are the experimental, calculated, and difference patterns, respectively. The black color tick marks indicate the peak positions of α-ferrite phase.

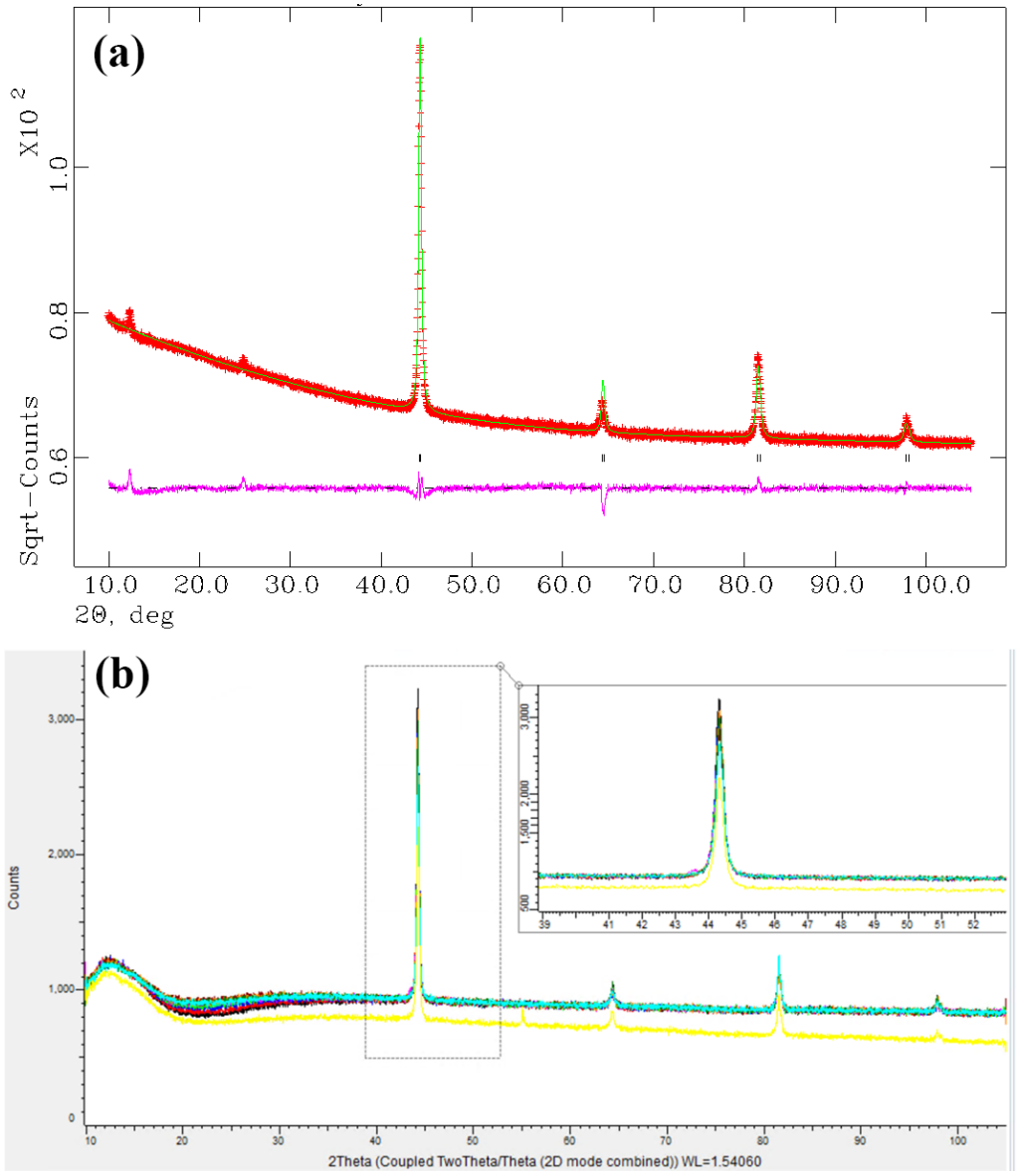

Figure A.3. XRD pattern of the transverse cut ShAPE extrudate together with its Rietveld fit. Red, green, and pink color are the experimental, calculated, and difference patterns, respectively. The black color tick marks indicate the peak positions of α-ferrite phase. (b) Micro-XRD patterns of the sample.

Appendix B – Supporting SEM data

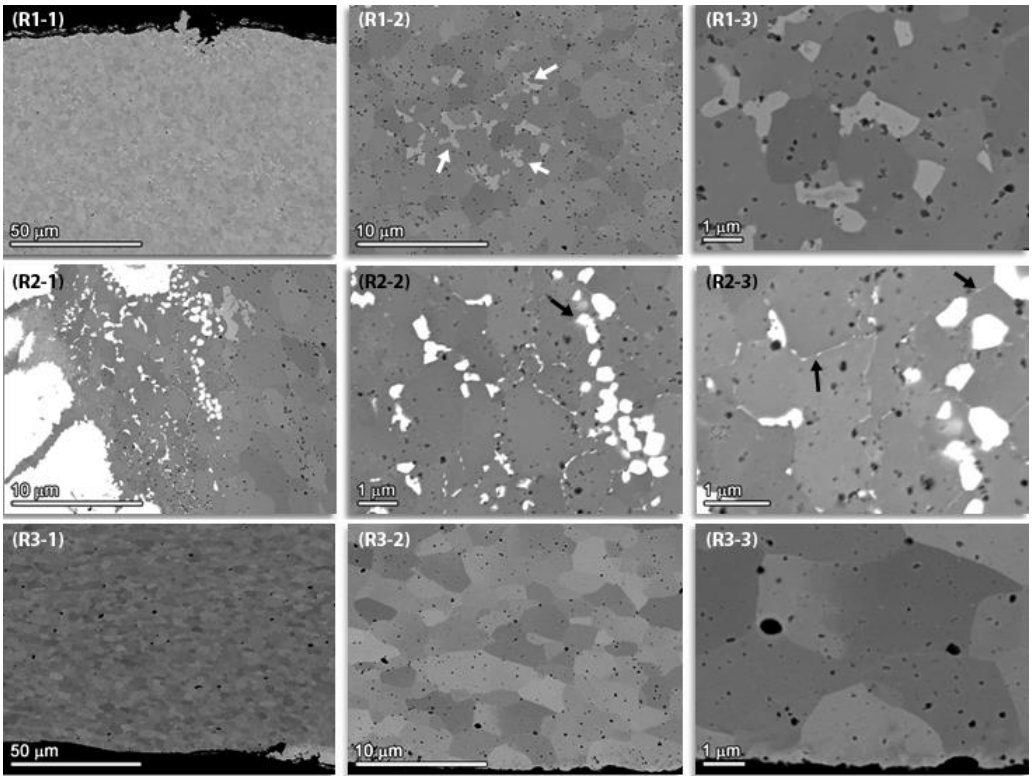

Figure B.1. SEM micrographs of start section of the PM2000 ShAPE extrudate cut along its longitudinal direction. R1-1 through R1-3 images show outer edge of the area highlighted with the bright-contrast Cr and W rich carbide precipitates together with dark-contrast areas rich with light elements such as Al. Similar features are also observed in the middle of the start section (R2-1 through R2-3), while inner part of the start section consists of a microstructure free of bright-contrast precipitates and lower level of dark-contrast precipitates.

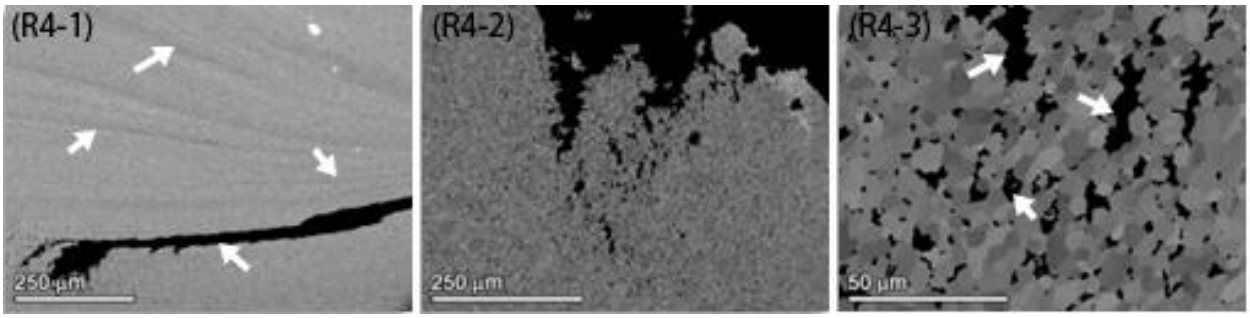

Figure B.2. SEM micrographs of start section of the PM2000 ShAPE extrudate cut along its longitudinal direction. R4-1 through R4-3 images show a crack area with mass flow lines and two other areas with a considerable number of voids.

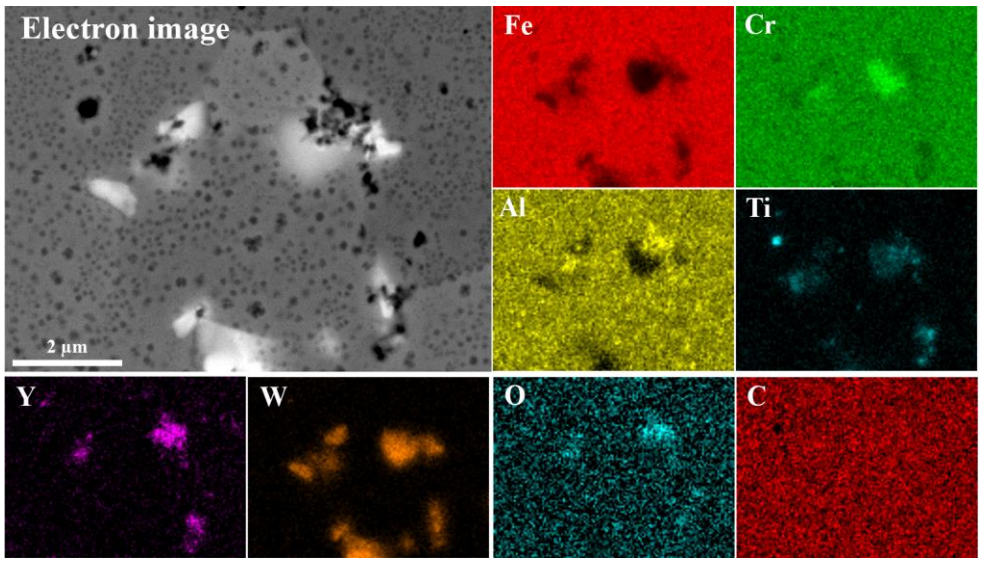

Figure B.3. SEM image and the corresponding EDS elemental maps of region 3 of the end section of ShAPE extrudate cut along longitudinal direction.

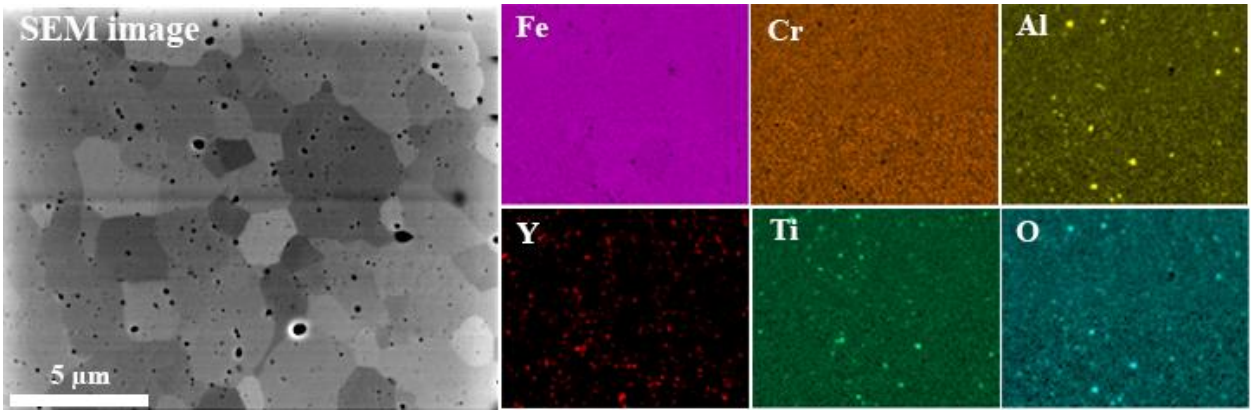

Figure B.4. SEM image and the corresponding EDS elemental maps of the ShAPE extrudate sample from near the middle section of the extrudate cut along its transverse direction.

Pacific Northwest National Laboratory

902 Battelle Boulevard
P.O. Box 999
Richland, WA 99354

1-888-375-PNNL (7665)

www.pnnl.gov